

---

# A modeling study of orographic convection and mountain waves in the landfalling typhoon *Nari* (2001)

Xiao-Dong Tang,<sup>a\*</sup> Ming-Jen Yang<sup>b</sup> and Zhe-Min Tan<sup>a</sup>

<sup>a</sup>Key Laboratory of Mesoscale Severe Weather of Ministry of Education, and School of Atmospheric Sciences, Nanjing University, China

<sup>b</sup>Department of Atmospheric Sciences, National Central University, Chung-Li, Taiwan

\*Correspondence to: X.-D. Tang, Key Laboratory of Mesoscale Severe Weather of Ministry of Education, School of Atmospheric Sciences, Nanjing University, Nanjing 210093, China.  
E-mail: xdtang@nju.edu.cn

---

In this study the characteristics of mountain-induced gravity waves (MGWs) and orographic convection in typhoon *Nari* (2001) and their impacts on the formation of orographic precipitation, as *Nari* moved across Taiwan's Central Mountain Range (CMR), are investigated by analyzing the cloud-resolving model simulation results. In the distant rain band, convective cells were triggered frequently on the steep windward slope of CMR and advected downstream. Simultaneously MGWs could exist on the lee side with stable environmental stratification. Three phases occurred in the MGWs–convection interaction, including the enhancement of MGWs and convection, breaking, and restoring of MGWs. When the convective cells and MGWs were superposed in (out of) phase, the amplitudes of both MGWs and convective cells were increased (decreased). The vertical wavelength of MGWs was also increased during the in-phase superposition, even inducing the further breaking of MGWs. For the formation of precipitation on the lee side, MGWs–convection interaction contributes on a smaller scale to offset the reduction effect from the larger-scale descending. Moreover, convective cells on the windward slope could contribute a large amount of cloud ice and snow particles aloft to seed hydrometeors over the lee side. More cloud water was produced by the MGWs–convection interaction when their amplitudes were increased during the in-phase superposition. Riming and coalescence processes were responsible not only for the windward-slope precipitation enhancement but also the secondary precipitation maximum over the lee side. Therefore, the MGWs–convection interaction could modify the structure of vertical motion and hydrometeors over the lee side, and then affect orographic precipitation when *Nari* passed the CMR.

As *Nari*'s eyewall encountered the northern CMR, the terrain generated long-lasting strong updrafts at the upslope, resulting in a doubled rainfall maximum to that in the no-terrain sensitivity experiment. The downdraft branch of the MGW produced a rain shadow on the lee side. Copyright © 2011 Royal Meteorological Society

**Key Words:** typhoon rain band; eyewall; orographic rainfall; precipitation microphysics

Received 15 February 2011; Revised 20 June 2011; Accepted 24 August 2011; Published online in Wiley Online Library 20 September 2011

**Citation:** Tang X-D, Yang M-J, Tan Z-M. 2012. A modeling study of orographic convection and mountain waves in the landfalling typhoon *Nari* (2001). *Q. J. R. Meteorol. Soc.* **138**: 419–438. DOI:10.1002/qj.933

## 1. Introduction

Mountain waves and orographic convection may play an important role in the formation of orographic precipitation through different mechanisms, such as upslope condensation (e.g. Hill *et al.*, 1981; Hill, 1983; Pandey *et al.*, 1999), seeder–feeder processes (e.g. Bergeron, 1965; Browning, 1980; Carruthers and Choullarton, 1983; Smith *et al.*, 2009a), upstream convection triggered or enhanced by terrain blocking (Grossman and Durran, 1984), windward slope triggering of convection (Smith *et al.*, 2009b), thermal triggering of convection, lee-side convergence (Mass, 1981), and lee-side enhancement of convection (Tripoli and Cotton, 1989). Among these studies, only a few have focused on the dynamical and microphysical aspects of mountain waves and orographic convection, which can substantially affect precipitation distribution and intensity.

For a conditionally unstable flow passing over a two- or three-dimensional mesoscale mountain ridge, three or four flow regimes, based on the moist Froude number ( $Fr_w$ ) and convective available potential energy (CAPE), are proposed by studies of idealized simulations (Chu and Lin, 2000; Chen and Lin, 2005a, 2005b). The flow regimes depicted the characteristics of propagation (upstream, downstream or quasi-stationary) and cloud types (convective or stratiform) of the simulated precipitation systems. An upward-propagating mountain wave can be produced by the strong basic flow in the higher  $Fr_w$  regimes (Chen and Lin, 2005a). Observational studies showed that in a strong cross-barrier flow with neutral to slightly unstable moist stratification, short-lived convective cells were intermittently triggered by the general uplift over the peaks on the windward side of a mountain range (Medina and Houze, 2003). The downslope winds on the lee side could also exhibit some aspects of mountain wave behavior (Medina *et al.*, 2005).

Moist static instability or nearly neutral stratification, and negative vertical shear of horizontal wind usually exist at low levels in the environment of landfalling typhoons (Blackwell, 2000; Chan and Liang, 2003). Convective cells can easily be triggered on the windward slope of a mountain range and then propagate downstream as the distant rain band of a typhoon is passing over a mountain range. In landfalling typhoons, mountain-induced gravity waves (MGWs) were also found, and could further transport precipitation particles to the lee side and lower levels (Misumi, 1996; Fudeyasu *et al.*, 2008). The impacts of mountain waves and convection over the steep terrain on precipitation are seldom discussed from a dynamical–microphysical perspective, especially in the landfalling typhoon environment. On the other hand, the inner core of a typhoon tends to have only marginal instability; it tends to be nearly conditionally symmetrically neutral with less static instability and lower CAPE than the large-scale environment of the typhoon (Houze, 2010). The effects of mountains on the vortex flow at different regions of a landfalling typhoon might be different.

The objective of this study was to investigate the essential features of MGWs and orographic convection in typhoon *Nari* (2001) over Taiwan, using the high-resolution simulation from Yang *et al.* (2008). That simulation reproduced reasonably well the storm track and structure during the landfall period, as well as the precipitation distribution and local rainfall maxima associated with Taiwan's orography. Based on this simulation, we will

examine how MGWs and orographic convection affect precipitation over the rugged terrain during *Nari*'s landfall on Taiwan. The following questions will be addressed in this study: (i) how does the propagation of orographic convective cells affect the evolution of mountain waves in the distant rain bands of typhoon *Nari*? (ii) How do mountain waves and orographic convection influence the microphysical processes and the formation of precipitation? (iii) What are the differences of mountain effects over different regions of a landfall typhoon, i.e. the distant rain band versus eyewall? Understanding these issues is important for advancing our knowledge of orographic precipitation, especially in a landfalling typhoon.

The remainder of the paper is organized as follows. The model set-up, the design of sensitivity experiment, and analysis method are introduced in section 2. Orographic convection and mountain waves in distant rain bands of *Nari* and their impacts on clouds and precipitation are examined in section 3. In section 4 the mountain effects over the inner core are discussed. Model sensitivity studies assist in analyzing the complex behaviors of orographic convection and mountain waves in these sections. Concluding remarks are given in the final section.

## 2. Methodology

### 2.1. Model set-up and experiment design

A non-hydrostatic version of the PSU–NCAR MM5 model (version 3.5; Dudhia, 1993; Grell *et al.*, 1994) is used to simulate typhoon *Nari* in Yang *et al.* (2008). The quadruply nested-grid (54/18/6/2 km) domains have 32  $\sigma$ -levels in the vertical, with the model top set at 50 hPa. The radiative boundary condition of Klemp and Durran (1983) was applied to the upper boundary in order to prevent gravity waves from being reflected and some spurious noise or energy build-up over topography. The physics options used in the simulation include the Medium-Range Forecast (MRF) model PBL parametrization (Hong and Pan, 1996), the atmospheric radiation scheme of Dudhia (1989), and the Grell (1993) cumulus parametrization. No cumulus scheme is used on the 6 km and 2 km grids. The Reisner *et al.* (1998) microphysics scheme is used, in which solved six prognostic variables of water species, including water vapor, cloud water, cloud ice, snow, rainwater, and graupel. See Yang *et al.* (2008) for further details of model set-up and the simulation results.

In this study, diagnosis of the control (CTL) simulation of Yang *et al.* (2008) has been performed with 2 km horizontal grid spacing and 2 min output interval for two periods. The first period is 0600–1800 UTC 16 September 2001, during which the sensitivity experiment with no terrains over Taiwan (NTR) in Yang *et al.* (2008) is used to examine the orographic modification on the rainfall and storm structure of a tropical cyclone just making landfall, especially for the corresponding mountain waves in the inner core. The second period is 0300–0500 UTC 18 September 2001, when the storm moved very slowly over southwestern Taiwan with nearly constant intensity (i.e. maximum wind speed about  $25 \text{ m s}^{-1}$ ; see Figures 4 and 5 in Yang *et al.*, 2008). In order to weaken orographic convection and then isolate the effect of mountain waves on the formation of precipitation on the leeside, we also conducted a sensitivity simulation in

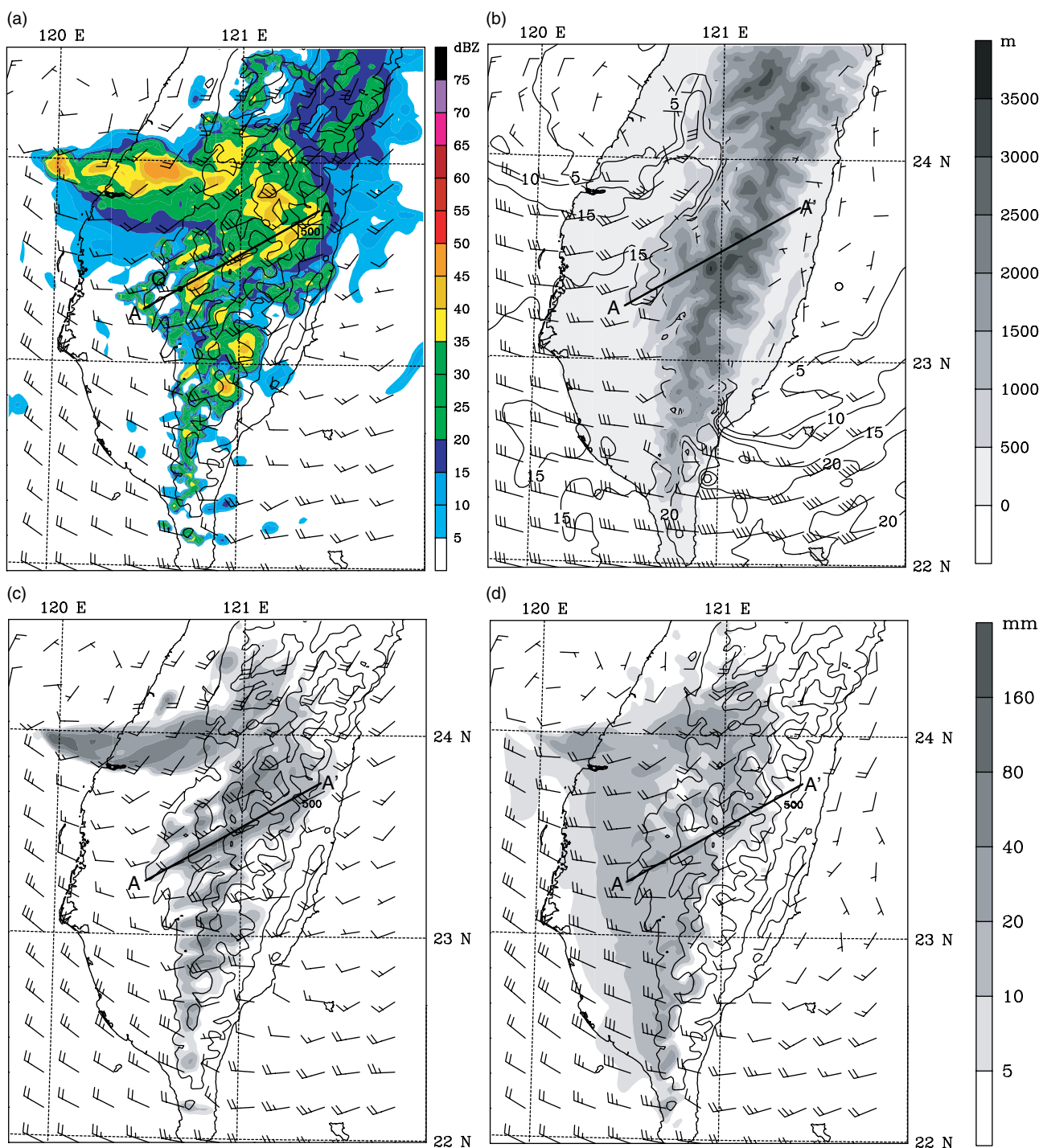


**Figure 1.** (a) Horizontal cross-section of vertical maximum radar reflectivity (colored) and horizontal wind barsbs at the 4 km level at 0400 UTC 18 September 2001 for the CTL run. (b) Horizontal wind barsbs and wind speeds (contoured every  $5 \text{ m s}^{-1}$ ) at the 1 km level at 0300 UTC 18 September 2001 for the CTL run, superposed with terrain height (shaded) at 500 m intervals. (c) The 2 h accumulated rainfall (shaded) during 0300–0500 UTC 18 September and horizontal wind barsbs at the 4 km level at 0500 UTC 18 September 2001 for the CTL run. (d) The same as (c) but for the NLH run. In (a), (c), (d), terrain height (thin solid) is contoured at 1000 m intervals (starting from 500 m height). The typhoon center is at the upper left corner of the figure.

which the latent heat release was turned off starting from 0300 UTC 18 September 2001. This run is referred to the ‘no latent heat’ (NLH) experiment.

2.2. Wavelet analysis

Morlet wavelet analysis is effective in the analysis of periodical phenomena like convection and gravity waves (Chagnon and Gray, 2008; Kuester *et al.*, 2008). The Morlet

wavelet function is defined as

$$\psi(x, s) = \pi^{-1/4} e^{6ix/s} e^{-\frac{1}{2}(x/s)^2},$$

where  $x$  is the independent spatial or temporal coordinate in the physical space, and  $s$  is a spectral parameter (e.g. a scale analogous to wavelength or period). Considering a time or spatial series  $f(x)$ , the continuous Morlet wavelet transform of  $f(x)$  is defined as a convolution of  $f(x)$  with the Morlet wavelet function. Similarly to the computation of Fourier

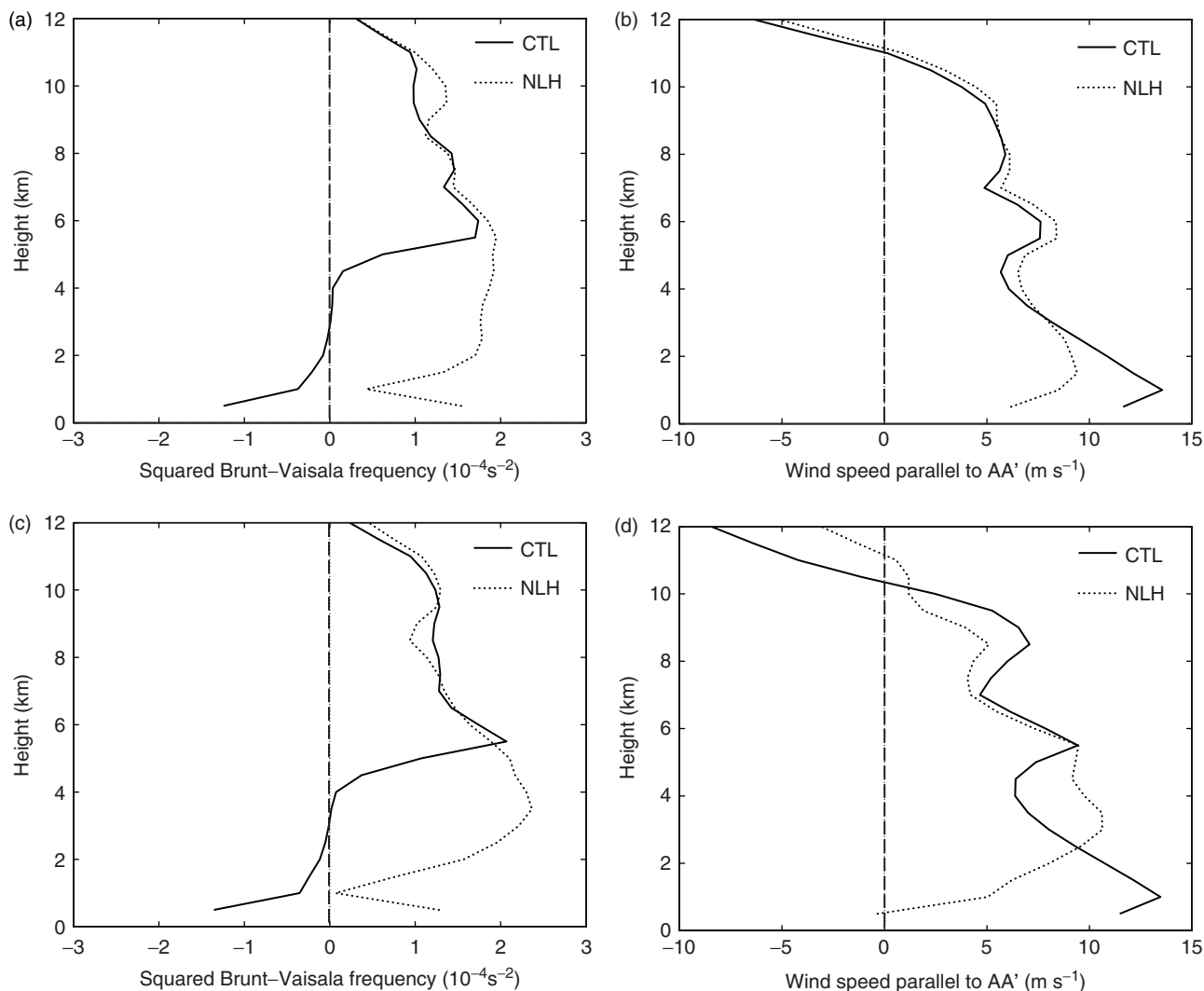


**Figure 2.** (a) 1 h averaged vertical profile at point A (see Figure 1) of moist (for the CTL run, solid line) and dry (for the NLH run, dotted line) squared Brunt–Väisälä frequency, and (b) wind component parallel to (positive (negative) is assumed to be into (out of) the cross-section) the cross-section AA' in Fig. 1 during 0300–0400 UTC 18 September 2001. (c) and (d) are as (a) and (b), but for 0400–0500 UTC 18 September 2001.

coefficients, the wavelet transform  $w(x, s)$  can be calculated as a function of wavelet scale and position in the spatial (or temporal) domain by computing the convolution at every fixed position by varying the wavelet scale  $s$ . Thus the wavelet power spectrum defined as  $|w(x, s)|^2$  shows the amplitude of any features versus the scale and how this amplitude varies with space or time. Wavelet analysis is more efficient than Fourier analysis in isolating the spectral properties of a phenomenon that is localized spatially or temporally. For detail of this method refer to Torrence and Compo (1998). The wavelet analysis is used in this study to find the dominant spatial (or temporal) scales of convective cells, mountain waves, precipitation, and the mountain range.

### 3. Orographic convection and mountain wave in distant rain band

Different types of rain bands exist in different regions of a typhoon, such as distant bands far from the typhoon center, principal and secondary rain bands in the inner core region, and the effects of mountains might be different since these rain bands have different internal dynamics. For example, the vertical structure of convection within distant rain bands is relatively unconstrained by the dynamics of the inner core

(Houze, 2010). Thus the effect of the Central Mountain Range (CMR) on the distant rain bands in *Nari* will be examined after *Nari*'s landfall on Taiwan.

#### 3.1. Upstream environment and convection triggering

During 0300–0500 UTC 18 September 2001, convective cells were generated frequently and then moved downstream in the distant rain bands of *Nari* when the tangential flows impinged on the CMR. Figure 1(a) is a snapshot that shows a convective cell generated near point Q with radar reflectivity greater than 45 dBZ. To examine the influence of CMR on the low-level circulation of *Nari*, Figure 1(b) displays the horizontal wind vector and wind speed in the CTL run at 1 km altitude at 0300 UTC 18 September 2001. With tremendous latent heat release associated with heavy rainfall, *Nari* still maintained constant intensity after landfall, so the wind speed was over  $10 \text{ m s}^{-1}$  at the windward upslope. Flow speed was hardly decreased from the coastline to the upstream plain of CMR, and was even increased a little near the immediate downstream of point A, with a magnitude of  $15 \text{ m s}^{-1}$  (Figure 1(b)).

*Nari*'s center was at the west of CMR in southern Taiwan during 0300–0500 UTC 18 September 2001. The 2 h accu-

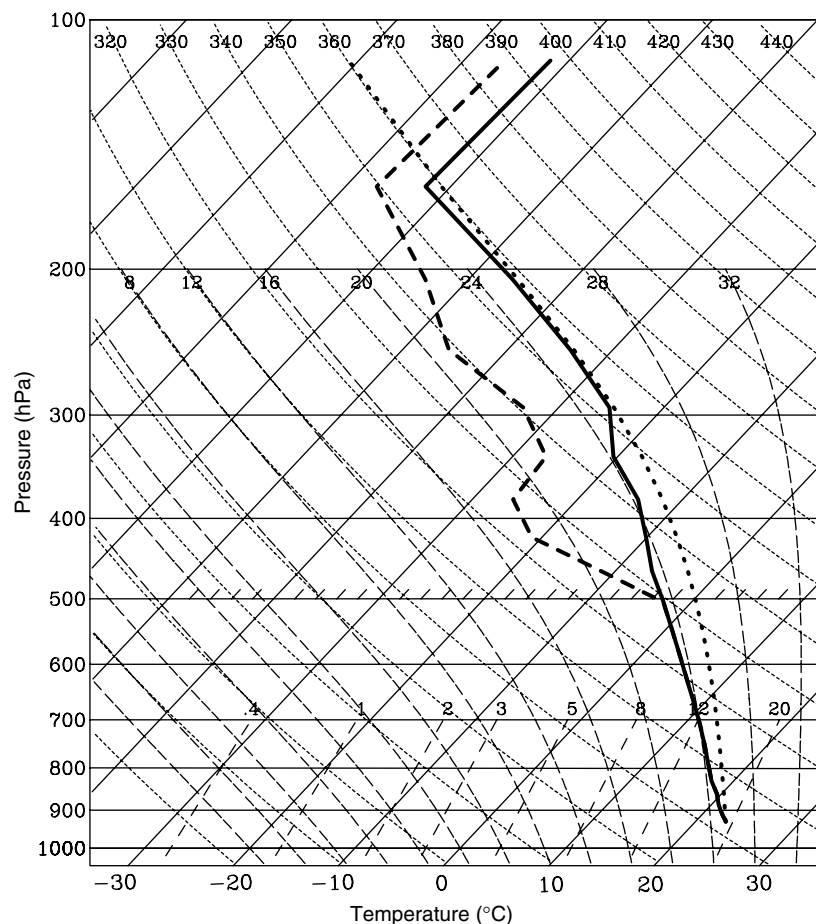


**Figure 3.** Temperature (solid) and dewpoint (dashed) sounding and temperature of a lifted parcel (dotted) at point Q in Figure 1(a) from the CTL run at 0300 UTC 18 September 2001.

mulated surface rainfall in Figure 1(c) showed banded features aligned with the prevailing cyclonic flows over the CMR; these banded precipitation features were mainly on the mountains with an altitude of over 500 m AMSL in southern Taiwan. For example, Line AA' is a centerline along one of the precipitation bands in the CTL run (Figure 1(a, c)). These rain bands were nearly parallel to horizontal flows over the top of mountain peaks (e.g. 4 km AMSL in Figure 1(a, c)). The 2 h maximum rainfall was over 80 mm and the maximum centers along these bands were all located on the windward (western) slope of CMR. Several rain bands even extended to the lee side of CMR. The banded distribution of precipitation was located at the smaller-scale ridges/valleys over the larger-scale upslope of CMR.

*Nari's* center in the NLH run was also at the west of CMR in southern Taiwan during the same time period. However, the 2 h accumulated rainfall was mainly distributed over the upslope of CMR and extended to the upstream plain of CMR and the maximum value was just close to 40 mm (Figure 1(d)). There were also some banded maxima of accumulated rainfall like those along AA', which was similar in terms of the precipitation pattern to that in the CTL run, although the amount was smaller and the location was further upwind (compare Figure 1(c) and (d)). The physical mechanisms for the differences in the precipitation amount and position between the CTL and NLH will be examined in detail in the following sections.

Figure 2(a) shows the 1 h averaged vertical profiles of moist (dry) squared Brunt–Väisälä frequency (SBVF) near

point A in the CTL (NLH) run during 0300–0400 UTC 18 September 2001. The moist Brunt–Väisälä frequency was calculated following Durran and Klemp (1982). In the CTL run, the moist SBVF is negative below 4 km, which indicates the convectively unstable stratification (Figure 2(a)). This is like the stratification conditions of idealized modeling studies of Chu and Lin (2000), and Chen and Lin (2005a, 2005b) and the observational study of IOP-2b case in Medina and Houze (2003). The air was saturated below 500 hPa with CAPEs of more than  $500 \text{ J kg}^{-1}$  at the upslope in the CTL run, rather than unsaturated in Chen and Lin (2005a), as shown by the sounding in Figure 3. The minimum convective (or potential) instability (defined by  $d\theta_e/dz$ ) was less than  $-10 \text{ K km}^{-1}$  in the lower levels and this buoyantly unstable layer could extend to 7 km altitude at the windward upslope (Figure 4(a)). Moreover, the 1 h averaged wind component along AA' was over  $10 \text{ m s}^{-1}$  below 2 km and there was a negative vertical shear in the layer of 1–4 km (Figure 2(b)). Thus convection was much more easily triggered by the upslope motion over the sudden-rising terrain than in the uniform basic flow in Chen and Lin (2005a). The updrafts at the upslope occurred in association with the latent heat release and in phase with the potential temperature perturbation, which corresponded to the feature of convective cells (Figure 4(b)). Since the latent heat release was turned off in the NLH run, the dry SBVF should be referred to in order to determine the stratification (Figure 2(a)), which was positive in the low level and reached its maximum of  $2.0 \times 10^{-4} \text{ s}^{-2}$  near the 6 km level.

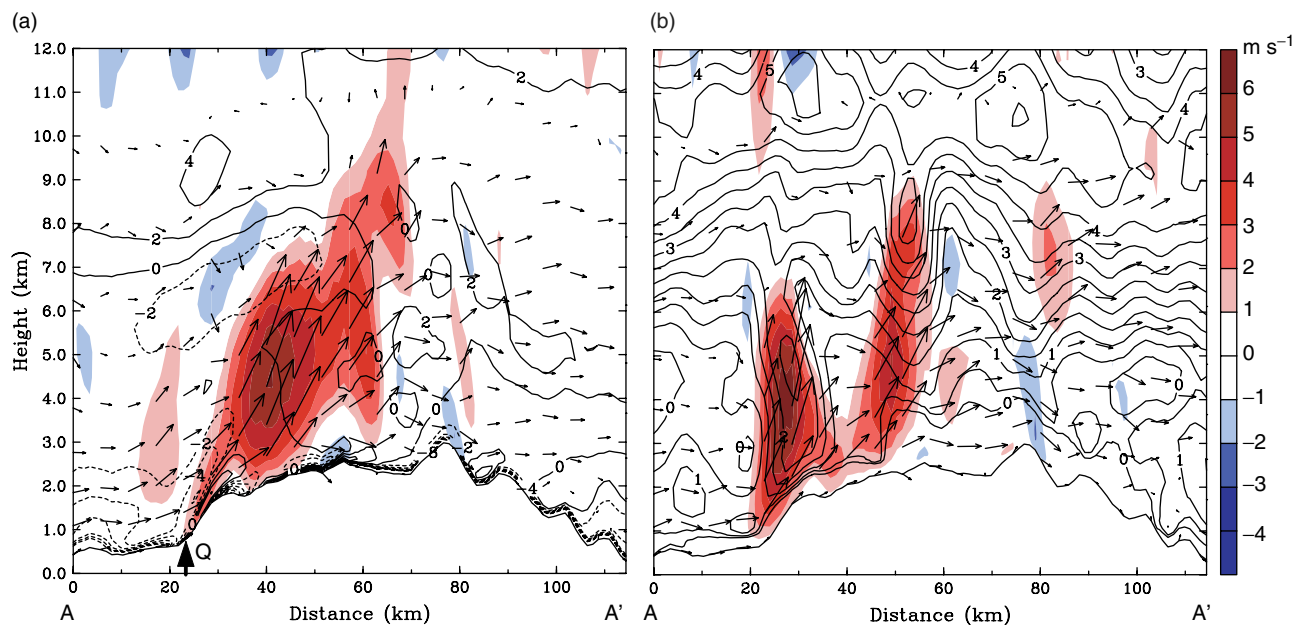


**Figure 4.** Vertical cross-sections along AA' in Figure 1(a) of (a) convective (or potential) instability (contoured at  $2 \text{ K km}^{-1}$ ), vertical velocity ( $\text{m s}^{-1}$ , colored), and along-plane wind vector at 0300 UTC 18 September 2001. (b) As (a) but for potential temperature perturbation (defined as the deviation from the initial value, contoured at  $0.5 \text{ K}$ ) and vertical velocity (colored) at 0348 UTC 18 September 2001.

Thus deep convection could not easily be triggered over the mountain under the environmental condition with stable stratification (for the whole vertical levels) and slow flow (at the lower levels) (Figure 2(a, b)). However, low-level shallow stratiform clouds and drizzle could be formed due to the convergence of onshore flow induced by the increased surface friction upstream of CMR (Figure 1(d)). During 0400–0500 UTC, the low-level stratification and flow speed changed very little compared with those 1 h earlier (0300–0400 UTC) in the CTL run, but the wind speed parallel to AA' decreased further below the 2 km level in the NLH run (Figure 2(c, d)). All these factors indicate that the orographic flows along the AA' cross-section in the CTL and NLH runs belonged to different flow regimes.

In brief, for the CTL run convective cells were easily produced in the convectively unstable air upstream of CMR and continued to interact with the mountain wave over the lee side. However, there was little convection and only mountain wave over the lee side since the air was convectively stable in the NLH run. We also found that the NLH run put the precipitation further upwind and much weaker than the CTL run (compare Figure 1(c) and (d)), because one role of latent heat release is to make the convection more organized, resulting in a relatively smaller rain area and stronger precipitation (Li *et al.*, 2007). The difference of precipitation patterns between the two runs is also related to the different flow regimes.

### 3.2. Propagation of convection and evolution of mountain waves

For the region near the main peak and lee side, the air is buoyantly stable in the middle and upper levels with the positive vertical gradient of equivalent potential temperature ( $\theta_e$ ) or potential stability (Figure 4(a)), so the mountain wave could occur on the lee side as in Medina *et al.* (2005) (Figure 4(b)). As convective cells were generated upslope and

advected downstream, they could influence the evolution of mountain waves near the peak.

#### 3.2.1. Verification and characteristics of convection and mountain waves

To clarify the influence of orographic convection on mountain waves, we first examine their respective characteristics by comparing results between the CTL and NLH runs. Figure 5(a) shows the Hovmöller diagram of vertical velocity at the altitude of 4 km AMSL along Line AA' for the 2 h period. The terrain height along AA' rises steeply near the location at 25 km (Figure 5(c)), where convective cells were triggered every 20–30 min. The convective updraft cells with horizontal scales of  $\sim 20 \text{ km}$  propagated northeastward along the windward slope between the horizontal distance of 20 and 70 km with a speed of  $\sim 13 \text{ m s}^{-1}$ , as estimated from the Hovmöller diagram and output animation. Some convective cells developed vigorously and extended to a higher level in the propagation along the windward upslope. Some convective cells even reached the height of 8 km for the horizontal distance at 35–45 km along AA' (Figure 6(a)). The maximum updraft of convective cells could exceed  $5 \text{ m s}^{-1}$  at the 8 km level before advecting to the main peak. A stationary downdraft–updraft couplet also occurred 15 km downstream near the mountain peak (at the distance of 77 km) at the 4 km level with a maximum amplitude of  $> 2 \text{ m s}^{-1}$  (Figure 5(a)). For the region near the main peak and lee side, the potential temperature perturbation was in quadrature with the vertical motion perturbation (Figure 4(b)), which corresponded to the feature of gravity waves (see Figure 12 of Yang and Houze, 1995). It is similar to an upward-propagating hydrostatic mountain wave produced by the strong basic flow in regimes III and IV (i.e. higher  $\text{Fr}_w$ ), identified in Chen and Lin (2005a). However, unlike regimes III and IV in Chen and Lin (2005a), there was no long-lasting orographic convective or stratiform precipitation system over the mountain peak in the CTL run,

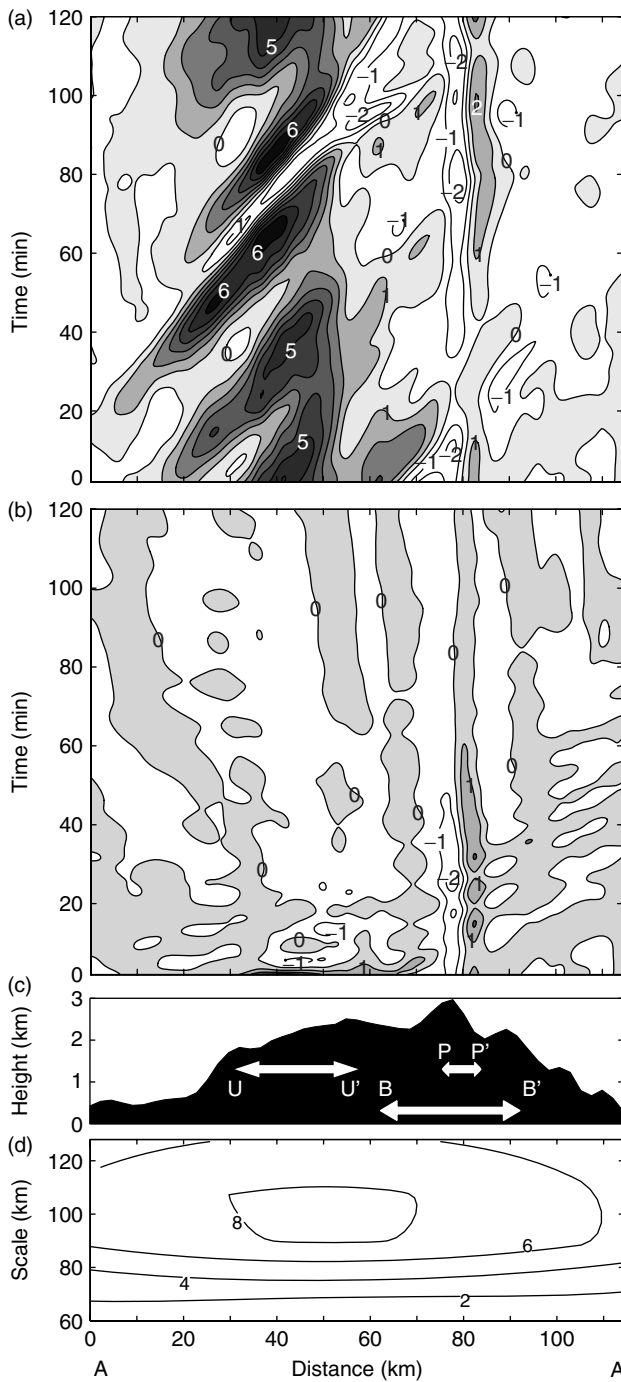


**Figure 5.** Time–space plot of vertical velocity along line AA' in Figure 1 at the 4 km level during 0300–0500 UTC 18 September 2001 for (a) the CTL run and (b) the NLH run. Contour interval is  $1 \text{ m s}^{-1}$  and positive values are shaded. (c) Height of the underlying terrain along line AA'. The white arrows UU' and PP' denote the focus areas in Figure 7(a, b). The white arrow BB' denotes the area shown in Figures 8, 11, and 12. (d) Morlet wavelet power spectrum (unit:  $\text{km}^2$ ) of the terrain height along line AA'.

which might be due to the more complex topography in the real world. At about 20, 30–50 and 80–100 min of the 2 h period the vertical ascending motion was increased for the horizontal distance of 80–90 km on the lee side (Figure 6(a)). For the NLH run the vertical motion was very weak on the windward upslope both in the lower and upper levels (Figures 5(b) and 6(b)). The mountain waves at the horizontal distance of 80 km still had considerable amplitudes even in the absence of orographic convection. During the first hour the vertical velocity amplitude was over

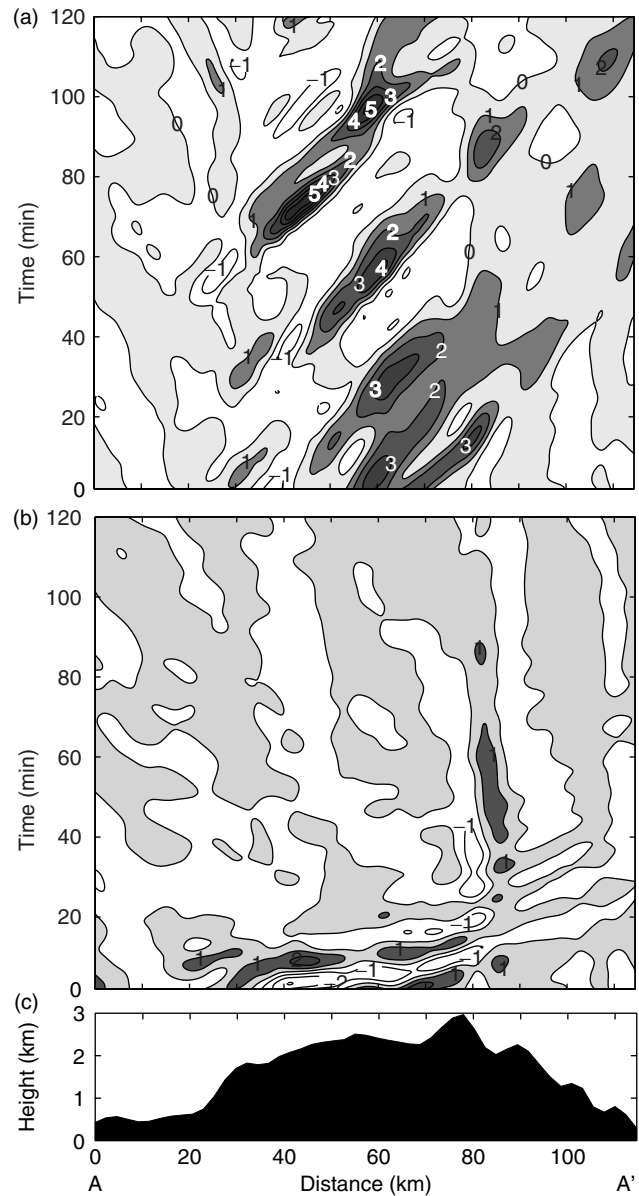


**Figure 6.** As Figure 5(a–c), but (a) and (b) are for the 8 km level.

$1 \text{ m s}^{-1}$  and decreased gradually in the second hour because of the weakening of the impinging flow (Figures 5(b) and 6(b)).

By performing the wavelet analysis of the spatial sequence in Figure 5(a) at every fixed time, the evolution of wavelet power spectra for the vertical velocity with the spatial scales during the 2 h period can be obtained. Figure 7(a) displays the evolution of mean power spectra for the horizontal distance between 30 and 55 km (i.e. location UU' in Figure 5(c)), where convective cells were generated and advected. There are two maxima of the spectra for most of the time and they correspond to two horizontal scales of 23 km and 90 km, respectively (Figure 7(a)). Figure 5(d) shows that there is only one maximum of the terrain height spectra from the wavelet analysis for all positions along line AA'; this maximum corresponds to a horizontal scale of  $\sim 90 \text{ km}$ , the dominant scale for terrain heights along line AA'. Consequently the spectrum with 90 km horizontal scale of vertical velocity in Figure 7(a) is possibly associated with orographic lifting along AA'. The horizontal scales of  $\sim 23 \text{ km}$  are associated with convective cells. The two

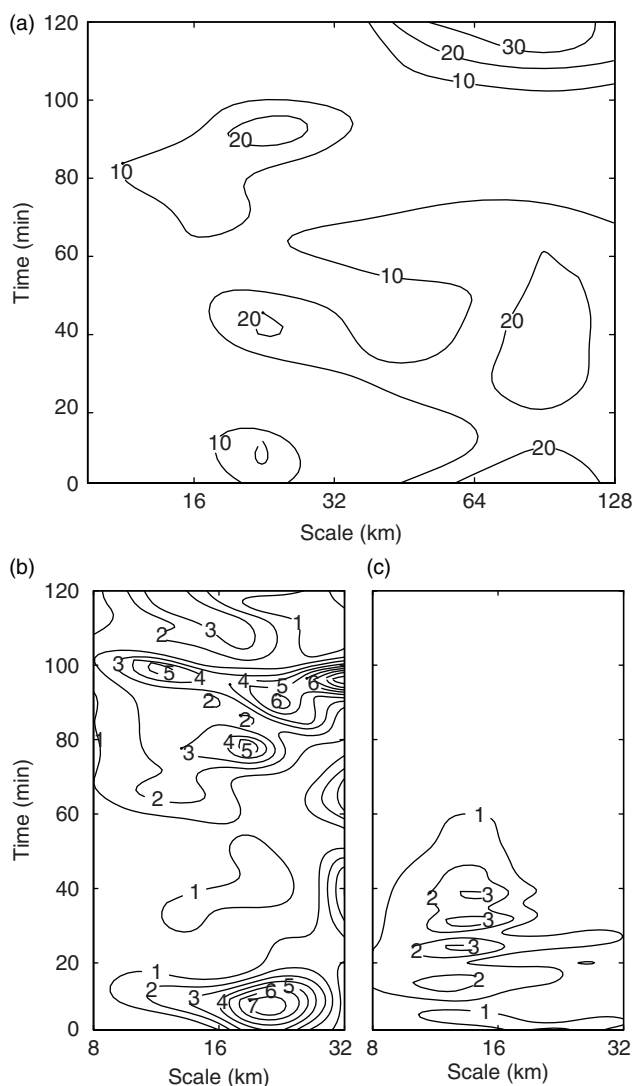


**Figure 7.** The evolution of Morlet wavelet power spectrum (unit:  $\text{m}^2 \text{s}^{-2}$ ) for the horizontal scale analysis of vertical velocity along line AA' at the 4 km level, averaged (a) between 30 and 55 km (i.e. UU' in Figure 5(c)) and (b) between 75 and 85 km (i.e. PP' in Figure 5(c)). (c) As (b) but for the NLH run.

modes of vertical velocities are similar to the two kinds of vertical velocities induced by orography and environmental instability proposed by Lin *et al.* (2001). The results of wavelet analysis for the NLH run also suggested the same two dominant horizontal scales along the windward upslope, but the wavelet power spectrum was much less than that in CTL run because of the weak vertical velocity (not shown).

Figure 7(b) shows the evolution of wavelet power spectra between 75 and 85 km near the mountain peak (i.e. the location PP' in Figure 5(c)) in the CTL run, where the interaction of mountain waves and orographic convection occurred. For the NLH run the mountain waves were hardly affected by convection, so the dominant horizontal wavelength of vertical motion at 4 km height is just for the mountain wave, which is between 12 and 16 km (Figure 7(c)). In the CTL run the dominant horizontal scale is about 20 km and the power spectrum is greater at  $t = 10$  min than that of broken mountain waves at  $t = 20$ – $40$  min (Figure 7(b)). After  $t = 60$  min, the mountain waves always existed, so the spectrum for the scale of  $\sim 12$  km was relatively large. Because the interaction between convection and mountain waves occurred over the

mountain peak and lee side, the dominant scale in the CTL run (20 km) is between that of convection (23 km) and that of mountain wave (12–16 km), which is slightly longer than that of the pure mountain wave in the NLH run. Especially around  $t = 100$  min, the wavelet power spectrum for the scale of  $\sim 12$  km nearly equals to that of  $\sim 20$  km scale (Figure 7(b)), since the amplitudes of mountain wave and convection are both large at this time (Figure 5(a)).

Vertical structures of mountain waves can be easily determined because mountain waves often occurred on the lee side along AA' (Figure 8(a)). The horizontal wavelength of mountain wave is  $\sim 12$  km and the vertical wavelength is  $\sim 4$  km, as estimated from the vertical velocity ( $w$ ) field. The maximum potential temperature ( $\theta$ ) perturbations are one quarter of a wavelength behind (to the left of) the updrafts in all levels below 10 km height (Figure 8(a)). On the contrary, the maximum  $\theta$  perturbations are one quarter ahead (to the right) of the maximum cross-barrier wind ( $u$ ) perturbations (parallel to AA' cross-section). There was a maximum of  $u$  perturbation near the surface of the lee slope and the other was at the 7 km level, which were both in phase with the two maximum updrafts. A minimum  $u$  perturbation was at the 4 km level, which was collocated with the maximum updraft. The distinct phase relationships among the  $w$ ,  $u$ , and  $\theta$  perturbations indicate that these are characteristics of internal gravity waves. The upstream tilt of the phase lines implies that the disturbance energy was propagating upward away from the mountain (Smith, 1979). The moist SBVF profile at the lee side of the peak (i.e. point L in Figure 8(a)) shows that air was nearly neutral above 8 km and there were two maxima of stability at  $z = 7$  km and the mountain surface on 0300 UTC 18 September (Figure 9). Consequently, the mountain waves were confined below 8 km (Figure 8(a)).

### 3.2.2. Influence of convection to mountain waves

Figure 8(a–d) shows that the horizontal wind component along BB' was close to zero near the surface and increased with height below 4 km at the windward upslope. The maximum wind of  $\sim 20 \text{ m s}^{-1}$  was at the layer between 5 and 7 km. This is because the latent heat released by orographic convection reduced the upstream blocking of the mountain and favored the 'flow over' regime by decreasing the effective static stability for the ascending saturated flow (Miglietta and Buzzi, 2001). When the upslope convective cells were advected downstream, the interaction between convective cells and MGWs began to occur near the peak (Figure 8(b)). The upward branches of MGWs were enhanced by latent heating. The convective updraft/downdraft cells gradually merged with the corresponding features of mountain waves (Figure 8(b)). On the windward upslope the convective cell E produced strong outflow on its foreside at the 6 km level and increased the cross-barrier flow to  $18 \text{ m s}^{-1}$  (Figure 8(a, b)). When the enhanced outflow approached the peak, great convergence occurred at the updraft branch of the mountain wave and vertical motion was strengthened due to mass continuity (Figure 8(b, c)). The amplitudes of mountain wave updrafts and downdrafts were increased by  $0.5 \text{ m s}^{-1}$  (Figure 8(b)). Increasing amplitude further caused the waves to break down, as seen from the nearly upright  $\theta$  contour of 320 K near point L (Figure 8(d)). The  $w$  phase lines gradually became vertically oriented (Figure 8(c, d)). The  $\theta$  field showed the evolution from the amplification of mountain

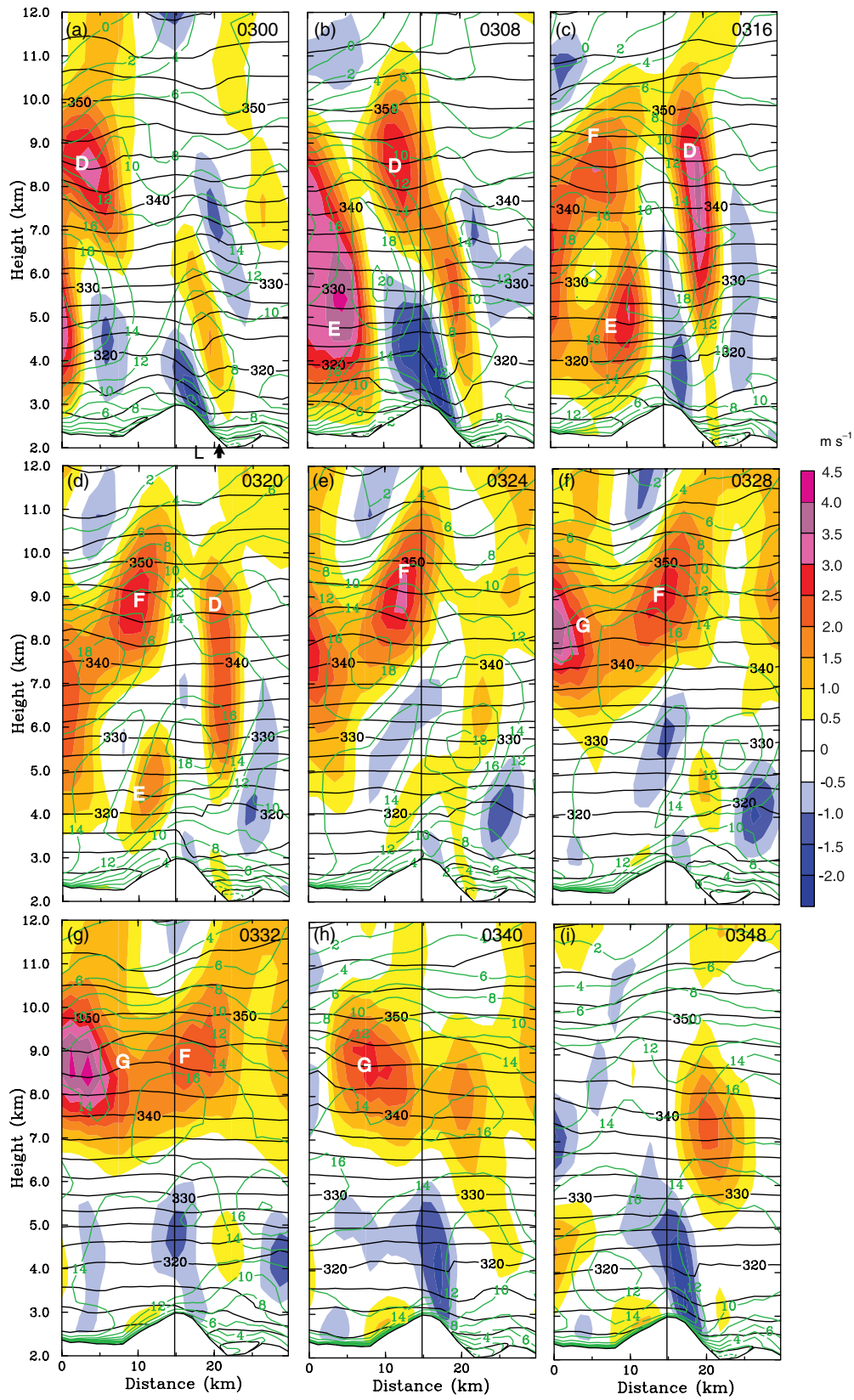


**Figure 8.** Vertical cross-sections along BB' in Figure 5(c) of vertical velocity (colored), horizontal wind component parallel to the cross-section (green contours at 2 m s<sup>-1</sup> intervals; solid/dashed line denotes positive/negative value) and potential temperature (black contours at 2.5 K intervals) for the CTL run. The UTC time is on the upper right corner of each panel. The thin line in the middle of each panel denotes the position of the mountain peak. The bold arrow in (a) shows the position of point L in Figure 9. Convective cells D, E, F, and G are indicated.

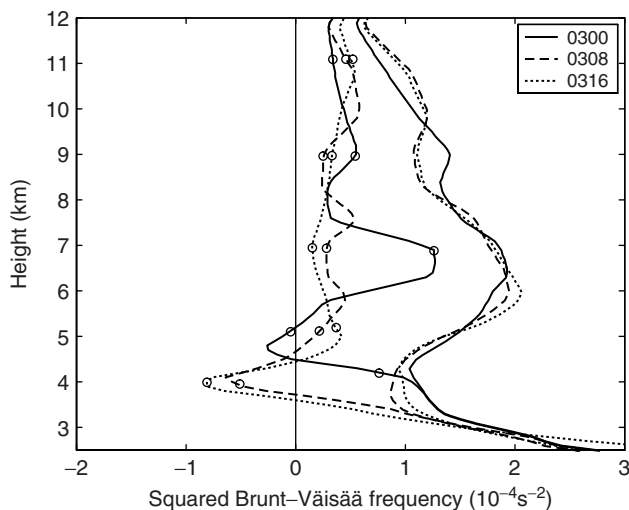


**Figure 9.** Moist (for the CTL run, with circles) and dry (for the NLH run, without circles) squared Brunt-Väisälä frequency profiles at point L in Figure 8 at 8 min intervals (time shown in the legend) from 0300 to 0316 UTC 18 September 2001.

waves to wave breaking (Figure 8(c, d)). When a  $\theta$ -isotherm became nearly vertically oriented at 0308 UTC 18 September, the flow became convectively unstable (Figure 8(b)). The moist SBVF on the lee side was decreased further below 4.5 km during the period of 0300–0316 UTC at point L (Figure 9). The variation of buoyancy frequency profile at the peak is similar to that at point L (not shown). Since the boundary layer was stable on the lee side with an unstable layer above (Figure 9), the hydraulic jump resulting from the mountain wave breaking made upward motion (mark D) strengthen further at the layer above 7 km (Figure 8(c, d)). There did not exist a region of wave overturning and upstream blocking during wave breaking, because the moist convection in this 3D simulation is different from the 2D dry case of wave breaking discussed in Lin and Wang (1996). At  $z = 3\text{--}5$  km, the 2 h averaged  $Fr_w$  is 0.5–1.5 at point A in the CTL run, so one might draw an analogy with regimes II, III and IV in Chen and Lin (2005a). However, no long-lasting convective or stratiform systems is located in the vicinity of the main mountain peak for the CTL run, and the weaker convergence associated with the hydraulic jump did not generate downstream-propagating convective systems at the lee side.

After the mountain wave broke down on the lee side, the low-level convective cell E approached the downdraft branch of the mountain wave at the peak, and the downdraft above the surface on lee side decreased gradually (Figure 8(c–e)). The upward motion of E on the windward slope was also weakened as a result of the superposition with the downdraft branch of the mountain wave (Figure 8(e, f)). The updraft marked F aloft at  $z = 9$  km was advected downstream and maintained its strength. Some downdraft was produced beneath updraft F due to the interaction of E and F with the mountain wave (Figure 8(d–f)). When the maximum horizontal flow ahead of E moved over the lee side, the updraft branch of the mountain wave began to weaken (Figure 8(d–f)). It is obvious that the upward motion of E broke the structure of the mountain wave further at  $t = 20\text{--}30$  min during the 2 h period (Figure 10(a)). The downdraft below F was connected with the MGW downdraft branch gradually (Figure 8(g, h)). The updrafts F and G were advected downstream to the lee side and the MGW

updraft branch was restored at 0348 UTC (Figures 8(i), 5(a) and 6(a)).

Three phases could be found in the interaction between orographic convection and MGWs from Figure 5(a) in the 2 h period. During the first 0–20 min, the mountain wave amplitude was increased by the effect of convection over the main peak and the maximum ascending exceeded  $3\text{ m s}^{-1}$  (Figures 5(a), 6(a), 8(a–d), 10(a)). The vertical wavelength was also increased during 0300–0320 UTC and the height of maximum updraft rose to over 8 km gradually with the approach of updraft aloft from convective cells. This is because the stability at about 6–7 km layer and below 4 km was decreased (Figure 9), which can be deduced from the dispersion relationship for gravity wave  $m^2 = N^2/\bar{u}^2 - k^2$  (Eq. (7.47) of Holton, 2004, where  $m$  and  $k$  are vertical and horizontal wave numbers, respectively). In the second phase ( $t = 20\text{--}40$  min), the amplitude of the mountain wave was decreased (Figure 8(e–g)). During 40–60 min, the mountain wave was restored and amplified again (Figure 8(h, i)). In the second hour, the variation of mountain wave amplitude was less than  $1\text{ m s}^{-1}$  and the downdraft branch was relatively steady, with the magnitude between 1 and  $2\text{ m s}^{-1}$  (Figure 5(a)).

Animation of the NLH output demonstrates that there was little orographic convection occurring over the windward slope along AA' during 0300–0500 UTC 8 September 2001. The vertically propagating mountain wave over the main peak along AA' had a vertical velocity amplitude of  $>1\text{ m s}^{-1}$  at about the 10 km level (Figure 11). The vertical wavelength is about 2 km in the lower level and is increased to 6 km in the upper level. The wave number 2 vertical structure of the mountain wave existed in the troposphere (Figure 11(a–i)). The vertical wavelength is shorter than that in the CTL run (Figure 10(a, b)), which is also consistent with the dispersion relationship  $m^2 = N^2/\bar{u}^2 - k^2$ , as a result of slower impinging flow speed ( $\bar{u}$ ; Figures 8 and 11) and greater SBVF ( $N^2$ ; Figures 2(a, c) and 9) in the NLH run. The horizontal wavelength is about 10 km in the low level. The vertical wavelength and amplitude of the mountain wave were basically unchanged during 0332–0348 UTC (Figures 10(b) and 11(g–i)). The vertical profiles of SBVF in Figure 9 show that whole levels were always stable, so wave breaking could not occur in the NLH run. In contrast to the CTL run, without strong orographic convection occurring at the upslope, the mountain wave in the NLH run could maintain its structure and strength (Figure 11(g–i)).

### 3.2.3. Impacts on clouds and precipitation

In section 3.2.2, it is clear that the interaction between convection and MGWs cloud changes the vertical motion over the lee side. How does the MGWs–convection interaction affect the distribution of hydrometeors and then the formation of orographic precipitations on the lee side? During IOP-2b from the Mesoscale Alpine Program (MAP) the airstream was potentially unstable with high Froude number impinging upon the upslope; convective cells embedded in the background lifting were favored to develop over the lower slopes, thus further enhancing the formation of clouds and precipitation on the lower windward slopes (Medina and Houze, 2003). In our CTL run, strong updrafts in convective cells lifted lots of water vapor upward to produce condensation on the windward upslope, thus increasing the cloud–water mixing ratio

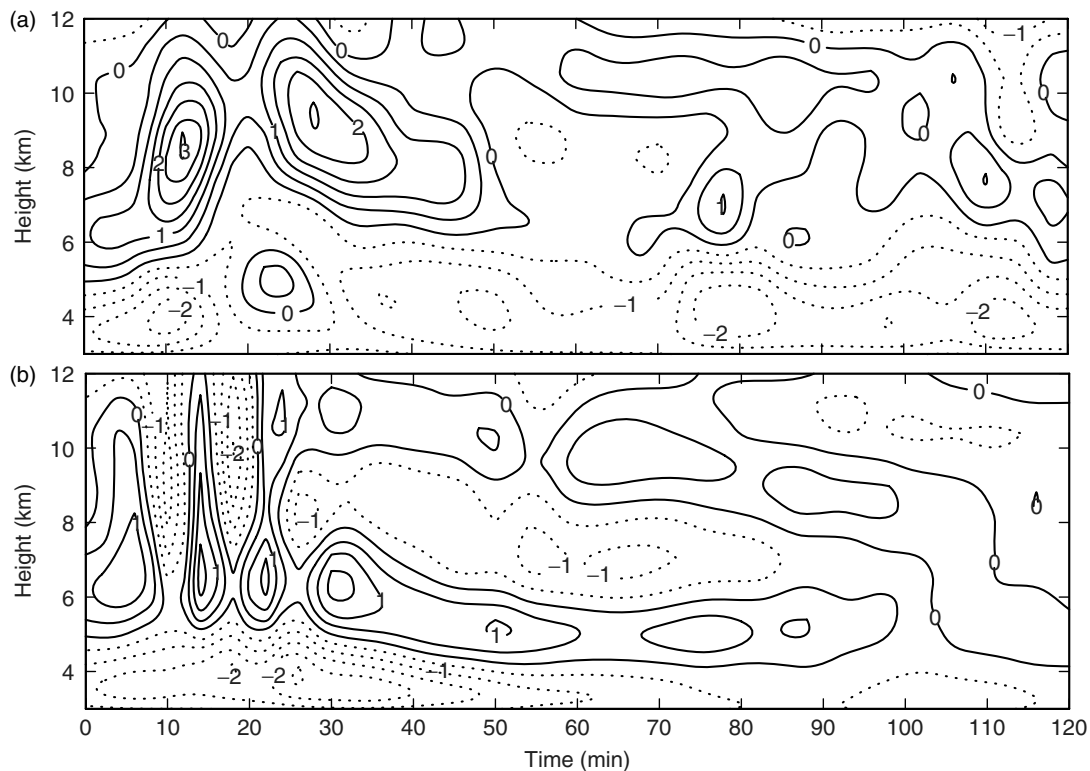


**Figure 10.** Height–time plot of vertical velocity at the mountain peak along the AA' during 0300–0500 UTC 18 September 2001 for the (a) CTL and (b) NLH runs. Solid/dotted line denotes positive/negative value.

(Figure 12(a)). Large graupel mixing ratio ( $>3 \text{ g kg}^{-1}$ ) existed over the region where maximum outflow occurred in the convective cell. Melting of graupel particles below the  $0^\circ\text{C}$  level (5 km) resulted in rainwater mixing ratio, and the drag force of rainwater induced strong downdraft. This enhancement mechanism of precipitation on the windward slope is consistent with that the fact the buoyant convective cells accentuate the coalescence and riming processes in IOP-2b described by Medina and Houze (2003). Cloud ice and snow particles were located at the middle-to-upper levels over the peak and lee side. The distribution of cloud ice was mostly above 10 km and its maximum mixing ratio occurred on the top of the updraft aloft from convection (Figure 12(a, b)). When the updraft D aloft was far from the mountain peak, the MGWs were not affected by the convection on the windward slope and the updraft branch of MGWs could not induce much condensation, so the mixing ratios of cloud water, graupel, and rainwater were relatively small (Figure 12(a)). After the updraft D approached the updraft branch of MGWs at 0312 UTC, its amplitude began to increase, so the cloud–water mixing ratio exceeded  $0.8 \text{ g kg}^{-1}$  between 5 and 10 km in the updraft branch of MGWs (Figure 12(b)). This effect of MGWs–convection interaction to the enhancement of cloud liquid water amounts over the lee side has never been examined closely in previous studies. At the same time the updraft D from convection provided larger vertical displacements than the MGW alone, leading to the seeding of a larger quantity of ice particles on the lee side. The riming process transformed snow to graupel particles, so the mixing ratio of graupel (snow) increased (decreased) (Figure 12(c)). Raindrops grew more rapidly by a coalescence process at lower levels. The rainwater mixing ratio in the downdraft branch of MGWs was increased by the melting of graupel,

and by the advection of upstream rainwater below updrafts D and E (Figure 12(a–c)). At the time of mountain wave breaking, the mixing ratios of the middle-level cloud water in the lee side were decreased because the MGW updraft intensity was weakened (Figure 12(d, e)). From the above analysis, it is clear that the interaction between the MGWs and orographic convection could modify the distribution of hydrometeors over mountain, and then enhance the coalescence and riming processes over the leeside slope.

The accumulated rainfall every 20 min along AA' is shown in Figure 13. During the periods of 0300–0320, 0320–0340, and 0340–0400 UTC, there was secondary maximum accumulated rainfall near the main peak (70–100 km) and drifting downstream (see marks J1–3 in Figure 13(a)), which was related to convective cell advection and interaction with the MGWs on the lee side. During 0400–0500 UTC there was also a similar process due to the MGWs–convection interaction (see marks K1–3 in Figure 13(a)). We further examine the relative contribution of different spatial scales to each 20 min accumulated rainfall along AA' based on wavelet filtering. The contribution of larger-scale mountain lifting mainly increases (reduces) rainfall (relative to the mean rainfall along AA') on the windward (lee) side. The contribution by convection and mountain wave or their interaction corresponds to the smaller-scale maxima (figure not shown). The small-scale rainfall maxima on the upslope were caused by 1–3 convective cells there (Figs. 5(a), 13). The small-scale maxima near the main peak and over the lee side (70–100 km) were affected by the interaction between convection and mountain wave (see marks J1–3 and K1–3 in Figure 13). The contribution from the smaller-scale MGWs–convection interaction could offset the reduction effect to rainfall from the larger-scale descending over the lee side.

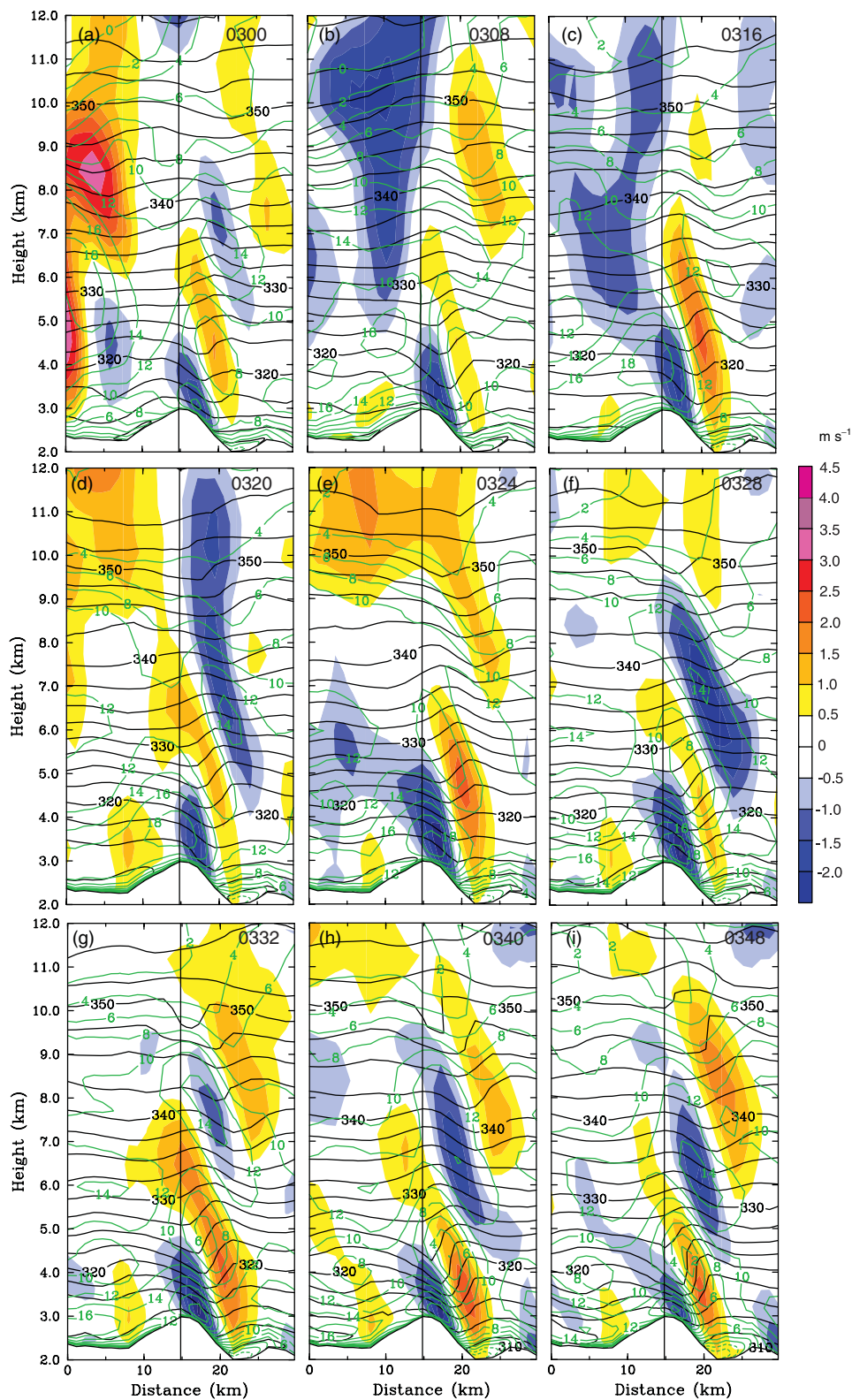
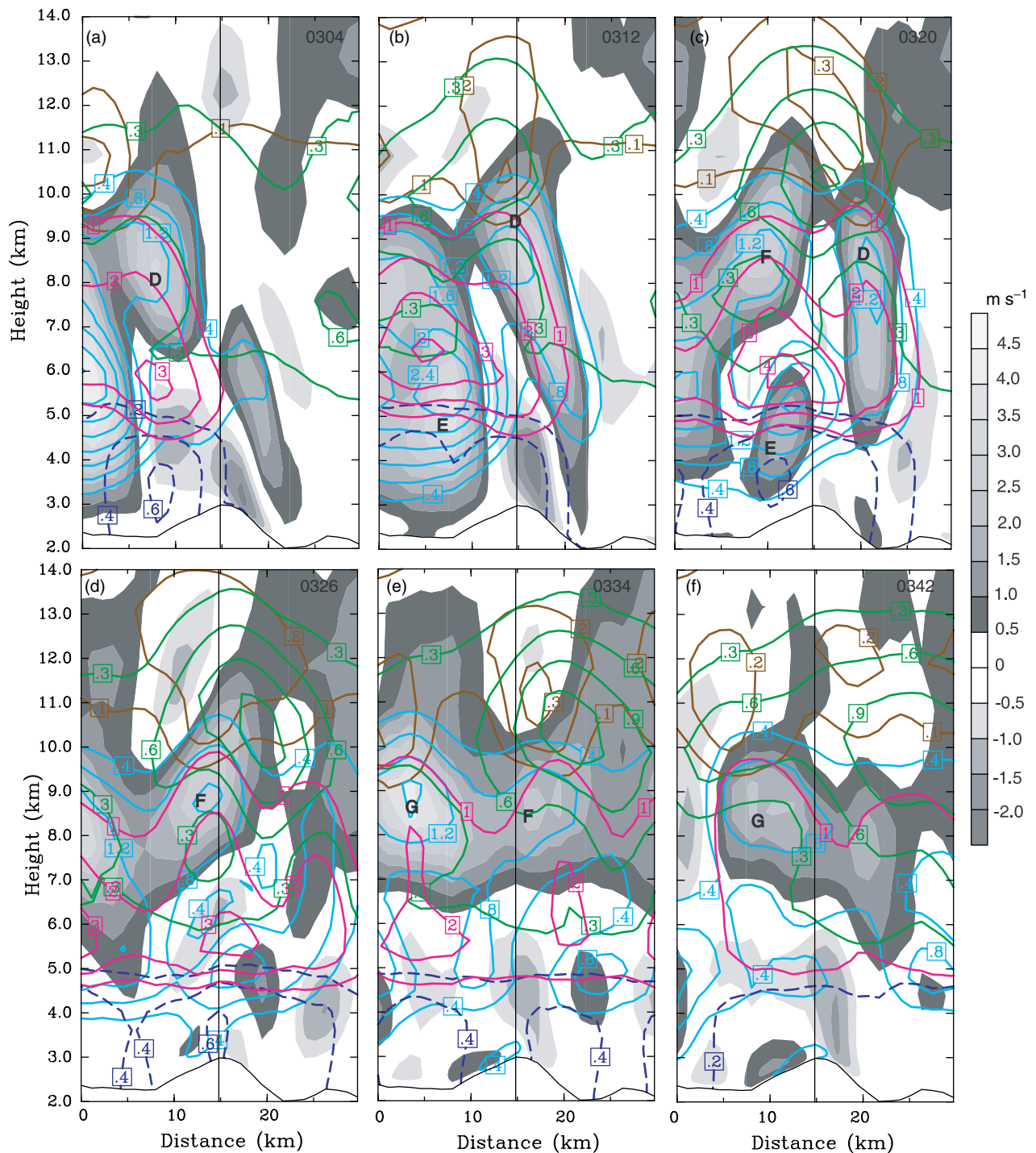


Figure 11. As Figure 8, but for the NLH run.

In the NLH run convection hardly existed over the upslope, so there were little precipitation hydrometeors there (figures not shown). Without strong convection ice particles could not be produced at the upper levels. Although there were steady mountain waves at the lee side, without the influence of convection these mountain waves alone could not produce precipitation because too little rainwater was formed.

#### 4. Mountain waves in the inner core

The inner core here is defined as the region of a typhoon, which is dynamically controlled by the cyclonic vortex circulation, following Houze (2010). We will further examine the mountain effect on the rain bands and eyewall in the inner core of *Nari*, especially for the corresponding mountain waves.



**Figure 12.** As Figure 8, but for the evolution of mixing ratios of cloud ice (brown:  $0.1 \text{ g kg}^{-1}$  intervals), cloud water (cyan:  $0.4 \text{ g kg}^{-1}$  intervals), snow (green:  $0.3 \text{ g kg}^{-1}$  intervals), graupel (magenta:  $1.0 \text{ g kg}^{-1}$  intervals), and rain water (dashed blue:  $0.2 \text{ g kg}^{-1}$  intervals), superposed with vertical velocity (shaded: light to dark gray denotes increasing downdraft or decreasing updraft) for the CTL run.

#### 4.1. Accumulated rainfall

In Yang *et al.* (2008) the comparison between the control run and no-terrain run (NTR) showed that their tracks (from the 6 km grid) were close before 1800 UTC 16 September 2001, but had large deviations afterwards because of the differences of environmental steering flows (see their Figure 18(d)). It is thus meaningful to compare the 12 h accumulated rainfall of the CTL storm and NTR experiment during 0600–1800 UTC 16 September 2001 at the initial landfall stage of *Nari*, when the two tracks are similar.

Figure 14(a, c) reveals that both the CTL and NTR runs (from the 2 km grid) produce an elongated heavy rainfall pattern over northern Taiwan to the left of the storm tracks. This is due to the controlling effect of southwesterly to southerly vertical shear vector in the large-scale flow; namely, heavier rainfall tends to occur on the downshear left side of the eyewall (cf. Figure 21(a, e) of Yang *et al.*, 2008, and Figure 3(a, b) of Yang *et al.*, 2011). However, the rainfall differences between the CTL and NTR indicate that the rainfall enhancement is mostly on the windward (western) side of Mt Snow, with a maximum of  $>800 \text{ mm}$ , and there

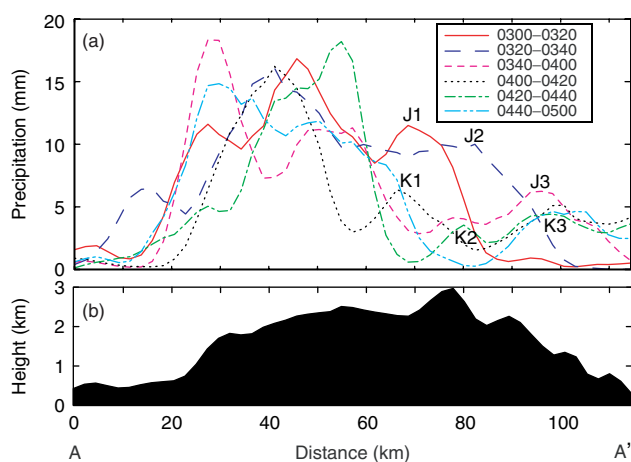


**Figure 13.** (a) The 20 min accumulated surface rainfalls during the periods as denoted in the legend using the UTC time format. Marks J1–3 and K1–3 are described in the text. (b) Underlying terrain along line AA'.

is some enhanced rainfall of >200 mm on the lee (eastern) side of Mt Snow over northeastern Taiwan (Figure 14(e)). The island-averaged 24 h accumulated rainfalls from the CTL run on 16 September 2001 doubled that of the NTR run because of the Taiwan terrain (see Table 5 of Yang *et al.*, 2008).

To clarify the influence of mountain waves to the rain bands and eyewall structure, Figure 14(b) shows the 2 h accumulated rainfall during 1100–1300 UTC 16 September 2001 in the CTL run (note that landfall time was 1000 UTC 16 September). It is interesting to compare the accumulated rainfall during 1000–1200 UTC 16 September in the NTR run (Figure 14(d)), because the landfall time of the NTR run was 1 h earlier than in the CTL run. It is important to note that along line NN' the maximum rainfall enhancement of >120 mm is upslope of the main peak; on the lee side, there is a rain shadow and a secondary maximum with a width of 10–20 km (Figure 14(b, f)). In the following subsection we will show that this rainfall pattern is associated with enhanced updraft on the upslope and mountain wave on the lee side.

#### 4.2. Terrain lifting and mountain wave

The *Nari* center gradually approached the main peak along NN' from the northeast during 1100–1300 UTC 16 September (Figure 14(a, b)). Both the principal rain band and eyewall passed over the main peak during this period, since the azimuthally averaged radius of maximum wind was 10–20 km (see Figure 8 of Yang *et al.*, 2011). Upslope of the main peak along NN' the steep terrain lifted the cyclonic flow to produce strong upward motion (Figure 15(a)), resulting in heavy precipitation and tremendous latent heat release (Figure 15(c)), and vertical motion was further enhanced by latent heating. Because of the intense low-level cyclonic flow, the precipitation particles would be advected downstream of the maximum updraft to some extent (Figure 15(c)), so the maximum of 2 h accumulated rainfall along NN' nearly coincided with the main peak (Figure 15(e)). Meanwhile, the MGWs were nearly stationary at the peak and the lee side, with a typical feature of downdraft–updraft couplet, on which the vertical velocity perturbation was in quadrature with the potential temperature perturbation (Figures 15(a) and 16). The downdraft branch of the mountain wave

was strong enough to enhance evaporation of cloud and precipitation hydrometeors, resulting in a sudden reduction of rainfall on the lee side of the main peak (Figure 15(c, e)). Radar reflectivity also showed a sharp decrease up to over 8 km level at about 20 km downwind of the downdraft (Figure 16(a–f)). The drying effect of the downdraft branch of the mountain wave on the lee side even helped to produce lower- $\theta_e$  air near the mountain surface, some of which intruded into the eye region later and led to the breakdown of the eyewall (see Figure 13 of Yang *et al.*, 2011). The small amount of rainfall (2 h maximum accumulation of about 50 mm) downwind of the rain shadow was associated with the updraft branch of the mountain wave (Figures 14(b) and 15(a, c, e)). The strong upward motion in the updraft branch consequently produced large radar reflectivity downwind (Figure 16(a–f)).

In comparison, there were no MGW features in vertical velocity or rainfall when the Taiwan terrain was totally removed (Figures 15(b, d) and 17). The wave number one asymmetry of 2 h accumulated rainfall (Figure 14(d)) was mainly due to the large-scale wind shear vector in the NTR run (see Figure 3(b) of Yang *et al.*, 2011). When principal rain bands and eyewall passed over the NN' cross-section, the rainfall would intensify there (see Figures 15(b, d) and 17(a–d)). When the eye passed through the NN' cross-section, the downdraft in the inner edge of the eyewall would decrease precipitation locally (Figure 17(e, f)). Note that these kinematic and rainfall features were only related to the internal dynamics of the typhoon in the NTR run.

In brief, the steep terrain doubles the rainfall at the main peak due to the increased latent heat release in the orographically enhanced upward motion when principal bands and eyewall were passing over the mountain peak (Figure 15(e)). The strong MGW downdraft branch produced the rain shadow by evaporation of precipitating hydrometeors on the lee side. The MGW updraft branch further contributed to the localized rainfall maximum (with width less than 20 km) on the lee side (Figures 14(b) and 15(e)).

## 5. Discussion and summary

In this study, we have examined the precipitation features in the distant rain band of typhoon *Nari* over Taiwan during 0300–0500 UTC 18 September 2001 and those in the inner core at the time of landfall during 1100–1300 UTC 16 September 2001. In the distant rain band, these precipitation features are caused by cyclonic flows over the smaller-scale ridges/valleys along the larger-scale upslope of CMR. We have investigated quantitatively the essential features of convective cells and MGWs and their interaction, and examined their impacts on the formation and distribution of precipitation over the CMR from a dynamical–microphysical perspective through a systematic comparison between the control run and the sensitivity experiments without latent heat release and terrain.

On the windward slope of CMR, convective cells were frequently triggered at the steep upslope in the environment with negative vertical shear of horizontal wind and low-level instability. The latent heat release by orographic convections helped the airstream to flow over the CMR rather than to flow around it. The horizontal scales of these convective cells were about 20 km. Consequently, convection modulated wind, cloud water and rainfall at smaller spatial and temporal

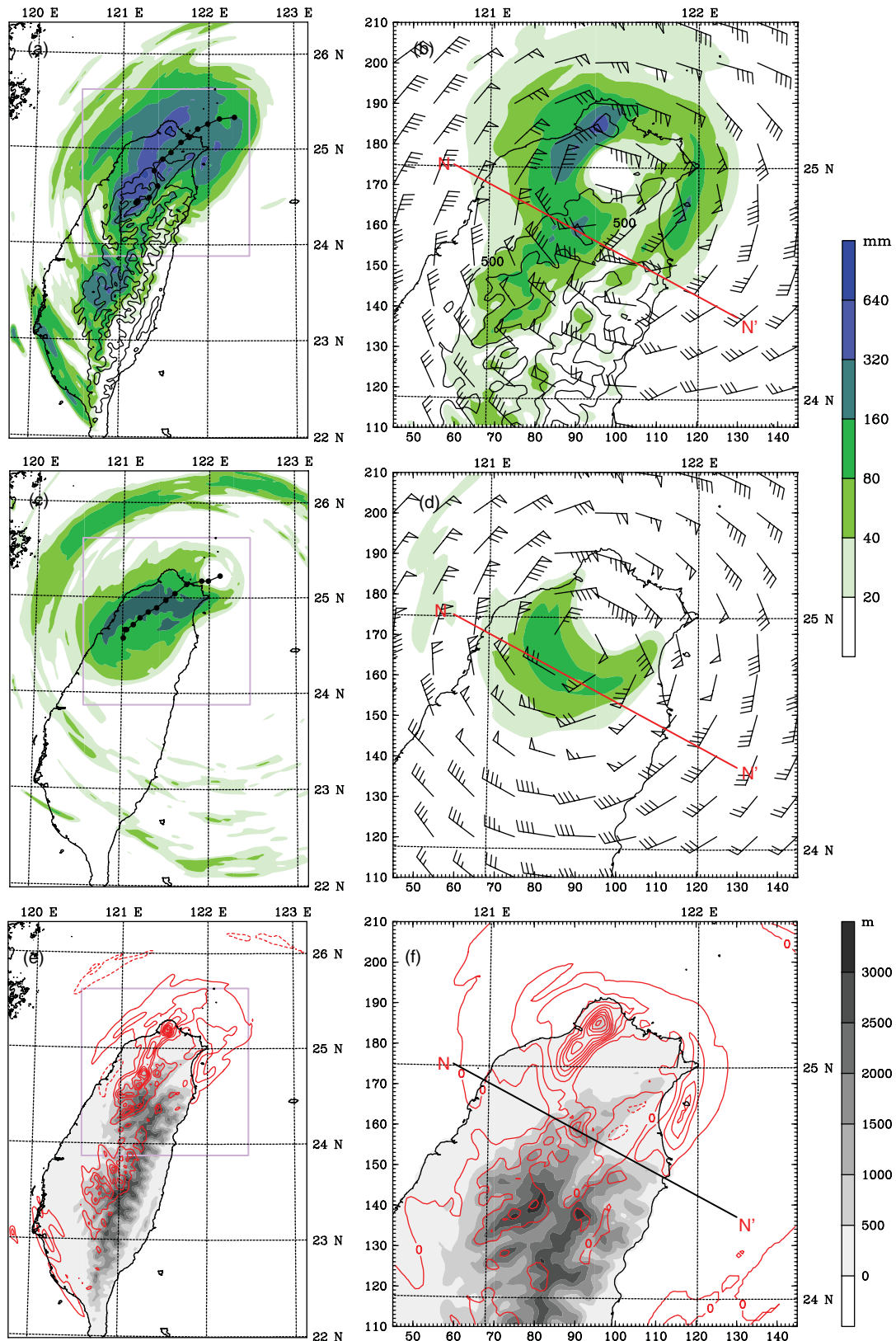


**Figure 14.** The 12 h accumulated rainfall (colored) during 0600–1800 UTC 16 September 2001 from the (a) CTL and (c) NTR runs. The simulated tracks during this period are indicated at hourly intervals. (e) is the difference of 12 h accumulated rainfalls between the CTL and NTR runs (contoured at 100 mm, solid/dashed line denotes positive/negative value and zero line is omitted). (b) The 2 h accumulated rainfall during 1100–1300 UTC 16 September 2001 and horizontal wind barbs at the 4 km level at 1300 UTC 16 September 2001 for the CTL run. (d) The 2 h accumulated rainfall during 1000–1200 UTC 16 September 2001 and horizontal wind barbs at the 4 km level at 1200 UTC from NTR run. (f) The difference of 2 h accumulated rainfalls between the CTL and NTR runs (contoured at 40 mm, solid/dashed line denotes positive/negative value and zero line is labeled). The terrain heights are contoured at 1000 m intervals (starting from the 500 m height) in (a) and (b), and shaded at 500 m intervals in (e) and (f). The magenta rectangles in (a), (c) and (e) denote the area of (b), (d) and (f). Horizontal positions of vertical cross-sections in Figures 15, 16 and 17 are indicated by lines NN' in (b), (d) and (f).

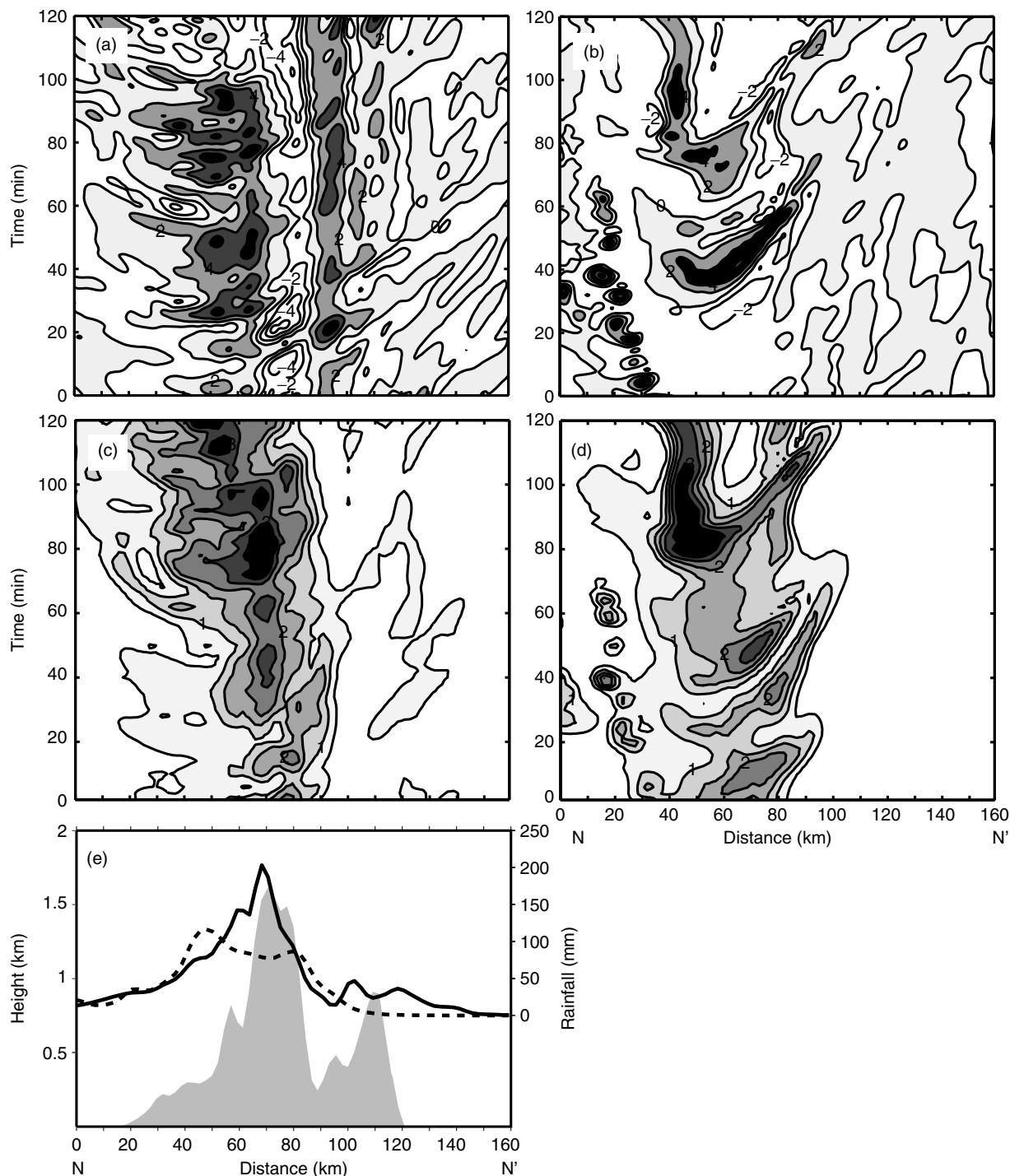


**Figure 15.** Time–space plot of (a) vertical velocity (contoured at  $2 \text{ m s}^{-1}$ ; positive values are shaded) at the 4 km level and (c) 2 min accumulated surface rainfall (contoured at  $0.5 \text{ mm}$ ) along Line NN' in Figure 14 during 1100–1300 UTC 16 September 2001 for the CTL run. (b) and (d) are the same as (a) and (c) but for the NTR run during 1000–1200 UTC 16 September 2001. (e) The 2 h accumulated surface rainfalls in the CTL run (solid line) and NTR run (dashed line) and the height of underlying terrain (shaded) along line NN' in Figure 14.

scales. Mountain waves also occurred on the lee side of mountain, whose horizontal wavelength was about 10 km. When the convective cells on the upslope were advected downstream and interacted with MGWs, the strong outflow from the upper part of the convective cells decelerated at the mountain wave updraft to produce strong convergence. The updraft branches of MGWs were sometimes enhanced by latent heat released by the convective cells advected downwind. Thus the in-phase superposition of convection and MGWs would increase the amplitude of MGWs on the lee side. At the same time, the vertical wavelength of MGWs

would also increase. The further increasing amplitude of MGWs caused its breakdown. When low-level upward motion was advected to the lee side and interacted with the downward branch of the MGWs, the amplitudes of MGWs were decreased. Moreover, the downdraft from convective cells could sometimes strengthen the downdraft branch of MGWs, so the mountain wave could be restored from the wave-breaking phase. Although the CTL run was similar to regimes II–IV in Chen and Lin (2005a), no long-lasting convective or stratiform systems can be found in the vicinity of the main mountain peak, possibly

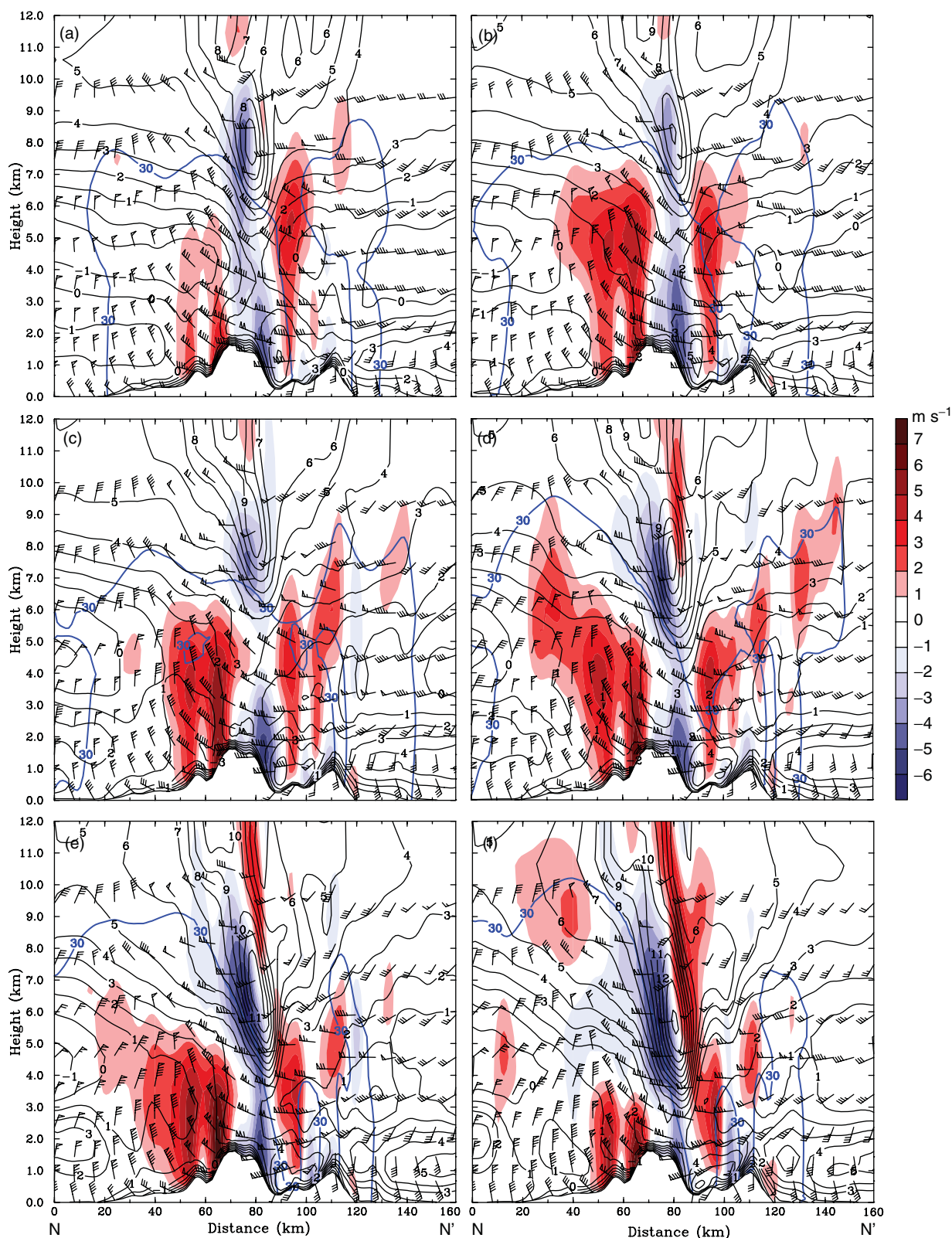


**Figure 16.** Vertical cross-sections of the 20 min averaged potential temperature perturbation (defined as the deviation from the initial value; black contoured at 1 K), vertical velocity ( $\text{m s}^{-1}$ , colored), horizontal wind barbs and 30 dBZ radar reflectivity contour (blue bold line) centered at (a) 1110 UTC, (b) 1130 UTC, (c) 1150 UTC, (d) 1210 UTC, (e) 1230 UTC and (f) 1250 UTC 16 Sept. 2001 for the CTL run.

because of the 3D mountain geometry. The convergence associated with the hydraulic jump was too weak to generate downstream-propagating convective systems on the lee side.

When the convective cells on the windward slope were triggered, the coalescence and riming processes resulted in

precipitation enhancement on the windward slope (Medina and Houze, 2003). At the same time, more cloud ice and snow particles were produced aloft over the peak and were advected downstream to seed the flow over the lee side. When the amplitudes of convective cells and mountain wave were increased in the positive interaction, more cloud water was

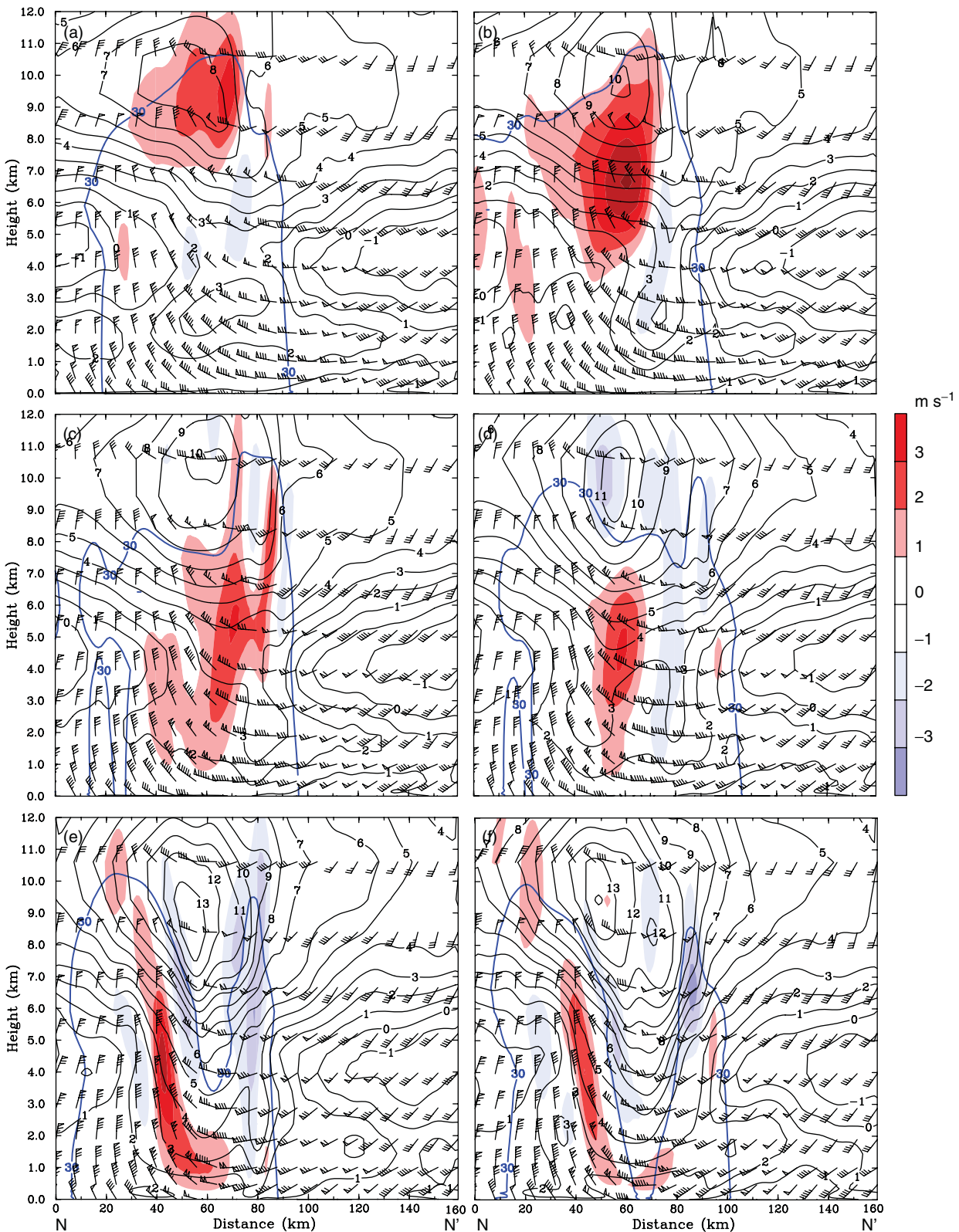


**Figure 17.** As Figure 16, but for NTR run, centered at (a) 1010 UTC, (b) 1030 UTC, (c) 1050 UTC, (d) 1110 UTC, (e) 1130 UTC and (f) 1150 UTC 16 Sept. 2001.

produced over the lee side, which favored the coalescence and riming mechanisms. The coalescence process at low level made raindrops grow much rapidly. Riming associated with snow particles aloft and supercooled cloud droplets at the middle levels produced many graupel particles. These two processes are responsible for the secondary precipitation maximum on the lee side. The small-scale

accumulated rainfall variations are contributed by both the larger-scale mountain lifting and the smaller-scale MGWs–convection interaction, which were comparably important. This indicates that the important interaction between the MGWs and orographic convection within a landfalling typhoon can modulate precipitation over the rugged terrain.

In a previous study of Hurricane Dean (2007) over Dominica island (Smith *et al.*, 2009a), it was found that the Dominica island was too narrow and the wind was too fast for convective cells to have time to form; orographic precipitation enhancement then was due to the seeder–feeder mechanism acting within a hurricane rain band. In our simulation results at the upslope of mountain, there is no low-level feeder ‘stratiform’ cloud because of the convectively unstable stratification with high CAPE in the environment for the distant rain band of *Nari*. The maximum wind traversing the mountain range is less than  $20 \text{ m s}^{-1}$  at the vertical level of 3 km, and the width of the mountain upslope is about 60 km, so the advective timescale is over 50 min, which is sufficient for cloud drops to grow to precipitation size after being generated at the foot of the mountain. In our current study, the mechanism for enhanced rainfalls over the mountain in the distant rain band is due to the terrain-induced convection rather than the ‘seeder–feeder’ mechanism.

Where the *Nari* eyewall and principal rain band passed over the northern CMR, the steep terrain greatly enhanced upward motion at the upslope, accompanied by the release of a tremendous amount of latent heat, leading to a doubled accumulated rainfall maximum near the main peak. The intense cyclonic flow within the inner core advected convective cells over the mountain peak to further downstream. The strong impinging flow produced a strong stationary downdraft branch of the mountain wave on the lee side, inducing an evident rain shadow. The updraft branch of the mountain wave also generated a localized rainfall maximum on the lee side.

It should be mentioned that the above conclusions are obtained from the cloud-resolving control and sensitivity simulations of a single typhoon case in Taiwan, in which some model deficiencies still exist. In the present study, we only investigated mountain waves and orography-induced convection in typhoon *Nari*. Inside the inner core, vortex Rossby waves and inertial gravity waves are also important in precipitation generation and propagation. Interaction between these waves and eyewall convection should be addressed in future studies.

### Acknowledgements

This research was supported by the National Basic Research Program of China (2009CB421500), the National Natural Science Foundation of China under Grants 41130964, 40705018, 40921160382 and the Chinese Special Fund for Public Service of Meteorology (GYHY201006004). MJY was also supported by the National Science Council of Taiwan under Grants NSC 97-2111-M-008-019-MY3, NSC 98-2625-M-008-002, and NSC 99-2625-M-008-005-MY3. We thank two anonymous reviewers for their constructive comments on an earlier version of the manuscript.

### References

- Bergeron T. 1965. ‘On the low-level redistribution of atmospheric water caused by orography’. In *Proceedings of the International Conference on Cloud Physics*, Tokyo, Japan. IAMAP/WMO; 96–100.
- Blackwell KG. 2000. The evolution of Hurricane Danny (1997) at landfall: Doppler-observed eyewall replacement, vortex contraction/intensification, and low-level wind maxima. *Mon. Weather Rev.* **128**: 4002–4016.
- Browning KA. 1980. Structure, mechanism, and prediction of orographically enhanced rain in Britain. In *Orographic Effects in Planetary Flows*, Hide R, White PW (eds). *GARP Publication Series*, Vol. 23, WMO; 85–114.
- Carruthers DJ, Choullarton TW. 1983. A model of feeder-seeder mechanism of orographic rain including stratification and wind-drift effects. *Q. J. R. Meteorol. Soc.* **109**: 575–588.
- Chagnon JM, Gray SL. 2008. Analysis of convectively-generated gravity waves in mesoscale model simulations and wind-profiler observations. *Q. J. R. Meteorol. Soc.* **134**: 663–676.
- Chan JCL, Liang X. 2003. Convective asymmetries associated with tropical cyclone landfall. Part I: f-plane simulations. *J. Atmos. Sci.* **60**: 1560–1576.
- Chen SH, Lin YL. 2005a. Effects of moist Froude number and CAPE on a conditionally unstable flow over a mesoscale mountain ridge. *J. Atmos. Sci.* **62**: 331–350.
- Chen SH, Lin YL. 2005b. Orographic effects on a conditionally unstable flow over an idealized three-dimensional mesoscale mountain. *Meteorol. Atmos. Phys.* **88**: 1–21.
- Chu CM, Lin YL. 2000. Effects of orography on the generation and propagation of mesoscale convective systems in a two dimensional conditionally unstable flow. *J. Atmos. Sci.* **57**: 3817–3837.
- Dudhia J. 1989. Numerical simulation of convection observed during the Winter Monsoon Experiment using a mesoscale two-dimensional model. *J. Atmos. Sci.* **46**: 3077–3107.
- Dudhia J. 1993. A nonhydrostatic version of the Penn State–NCAR mesoscale model: validation tests and simulation of an Atlantic cyclone and cold front. *Mon. Weather Rev.* **121**: 1493–1513.
- Durran DR, Klemp JB. 1982. On the effects of moisture on the Brunt–Väisälä frequency. *J. Atmos. Sci.* **39**: 3846–3879.
- Fudeyasu H, Kuwagata T, Ohashi Y, Suzuki SI, Kiyohara Y, Hozumi Y. 2008. Numerical study of the local downslope wind ‘Hirodo-kaze’ in Japan. *Mon. Weather Rev.* **136**: 27–40.
- Grell GA. 1993. Prognostic evaluation of assumptions used by cumulus parameterizations. *Mon. Weather Rev.* **121**: 764–787.
- Grell GA, Dudhia J, Stauffer DR. 1994. ‘A description of the fifth-generation Penn State/NCAR Mesoscale Model (MM5)’. *NCAR Tech. Note NCAR/TN-398STR*.
- Grossman PA, Durran DR. 1984. Interaction of low-level flow with the Western Ghat Mountains and offshore convection in the summer monsoon. *Mon. Weather Rev.* **112**: 652–672.
- Hill FF. 1983. The use of average annual rainfall to derive estimates of orographic enhancement of frontal rain over England and Wales for different wind directions. *J. Climatol.* **3**: 113–129.
- Hill FF, Browning KA, Bader MJ. 1981. Radar and rain gauge observations of orographic rain over south Wales. *Q. J. R. Meteorol. Soc.* **107**: 643–670.
- Holton JR. 2004. *An Introduction to Dynamic Meteorology*. Academic Press: London.
- Hong SY, Pan HL. 1996. Nocturnal boundary layer vertical diffusion in a medium-range forecast model. *Mon. Weather Rev.* **124**: 2322–2339.
- Houze RA. 2010. Clouds in tropical cyclones. *Mon. Weather Rev.* **138**: 293–344.
- Klemp JB, Durran DR. 1983. An upper boundary condition permitting internal gravity wave radiation in numerical mesoscale models. *Mon. Weather Rev.* **111**: 430–444.
- Kuester MA, Alexander MJ, Ray EA. 2008. A model study of gravity waves over Hurricane Humberto (2001). *J. Atmos. Sci.* **65**: 3231–3246.
- Li YY, Hang W, Zhao JZ. 2007. Roles of mesoscale terrain and latent heat release in typhoon precipitation: a numerical case study. *Adv. Atmos. Sci.* **24**: 35–43.
- Lin YL, Wang TA. 1996. Flow regimes and transient dynamics of two-dimensional stratified flow over an isolated mountain ridge. *J. Atmos. Sci.* **53**: 139–158.
- Lin YL, Chiao S, Wang TA, Kaplan ML, Weglarz RP. 2001. Some common ingredients for heavy orographic rainfall. *Weather Forecast.* **16**: 633–660.
- Mass CF. 1981. Topographically forced convergence in western Washington state. *Mon. Weather Rev.* **109**: 1335–1347.
- Medina S, Houze RA. 2003. Air motions and precipitation growth in Alpine storms. *Q. J. R. Meteorol. Soc.* **129**: 345–372.
- Medina S, Smull BF, Houze RA, Steiner M. 2005. Cross-barrier flow during orographic precipitation events: results from MAP and IMPROVE. *J. Atmos. Sci.* **62**: 3580–3598.
- Miglietta MM, Buzzi A. 2001. A numerical study of moist stratified flows over isolated topography. *Tellus* **53A**: 481–499.
- Misumi R. 1996. A study of the heavy rainfall over the Ohsumi Peninsula (Japan) caused by Typhoon 9307. *J. Meteorol. Soc. Japan* **74**: 101–113.
- Pandey GR, Cayan DR, Georgakakos KP. 1999. Precipitation structure in the Sierra Nevada of California during winter. *J. Geophys. Res.* **104**: 12019–12030.

- Reisner J, Rasmussen RJ, Bruijtes RT. 1998. Explicit forecasting of supercooled liquid water in winter storms using the MM5 mesoscale model. *Q. J. R. Meteorol. Soc.* **124**: 1071–1107.
- Smith RB. 1979. The influence of mountains on the atmosphere. *Adv. Geophys.* **21**: 87–230.
- Smith RB, Schafer P, Kirshbaum D, Regina E. 2009a. Orographic enhancement of precipitation inside Hurricane Dean. *J. Hydrometeorol.* **10**: 820–831.
- Smith RB, Schafer P, Kirshbaum DJ, Regina E. 2009b. Orographic precipitation in the tropics: experiments in Dominica. *J. Atmos. Sci.* **66**: 1698–1716.
- Torrence C, Compo GP. 1998. A practical guide to wavelet analysis. *Bull. Am. Meteorol. Soc.* **79**: 61–78.
- Tripoli GJ, Cotton WR. 1989. Numerical study of an observed orogenic mesoscale convective system. Part I: Simulated genesis and comparison with observations. *Mon. Weather Rev.* **117**: 273–304.
- Yang MJ, Houze RA. 1995. Multicell squall-line structure as a manifestation of vertically trapped gravity waves. *Mon. Weather Rev.* **123**: 641–661.
- Yang MJ, Zhang DL, Huang HL. 2008. A modeling study of Typhoon *Nari* (2001) at landfall. Part I: The topographic effects. *J. Atmos. Sci.* **65**: 3095–3115.
- Yang MJ, Zhang DL, Tang XD, Zhang Y. 2011. A modeling study of Typhoon *Nari* (2001) at landfall: 2. Structural changes and terrain-induced asymmetries. *J. Geophys. Res.* **116**: D09112, DOI: 10.1029/2010JD015445.